



# Accretion of Meteoric Organic Matter at the Surface of Mars and Potential Production of Methane by Ultraviolet Radiation

Juan Diego Carrillo-Sánchez<sup>1,2</sup>, John M. C. Plane<sup>3</sup>, Diego Janches<sup>2</sup>, and Gerónimo L. Villanueva<sup>4</sup>

<sup>1</sup> Department of Physics, Catholic University of America, 620 Michigan Avenue NE, Washington, DC 20064, USA; [juandiego.carrillosanchez@nasa.gov](mailto:juandiego.carrillosanchez@nasa.gov)

<sup>2</sup> ITM Physics Laboratory, NASA/Goddard Space Flight Center, Code 675, 8800 Greenbelt Road, Greenbelt, MD 20771, USA

<sup>3</sup> School of Chemistry, University of Leeds, Woodhouse Lane, Leeds LS2 9JT, UK

<sup>4</sup> Solar System Exploration Division, NASA/Goddard Space Flight Center, Code 690, 8800 Greenbelt Road, Greenbelt, MD 20771, USA

Received 2024 April 9; revised 2024 May 24; accepted 2024 June 1; published 2024 July 17

## Abstract

In this study, a comprehensive model of the meteoric organic cycle on Mars for the current geological period is developed, which characterizes the ablation of exogenous organic matter in the upper atmosphere, the accretion of intact carbon at the surface, and the potential production of methane by UV photolysis from the surface reservoir. The model accounts for both the latitudinal and seasonal variation of the meteoroids' input from the most relevant populations in the inner solar system. A recent version of the University of Leeds Chemical Ablation Model, which includes a semiempirical model to describe the pyrolysis kinetics of the meteoric organic matter, is then combined with this meteoroid input function and a semiempirical model that quantifies the UV production of methane. The minimum and maximum accretion rates of organics are between 18 and 90 kg sol<sup>-1</sup> at aphelion and 45–134 kg sol<sup>-1</sup> at the first crossing of the ecliptic plane. The resulting mixing ratios of carbon, in the top 200 μm of the surface layer, range from 0.09–0.43 ppm at 20°N to 4.8–8.9 ppm around the south pole. To be consistent with the methane upper limit of 0.02 ppbv measured by the NOMAD instrument on the ExoMars Trace Gas Orbiter, the UV photolysis yields for methane production need to be around 3% assuming a meteoric carbon content in comets of 25.6 wt% and an atmospheric lifetime of methane of 329 Earth yr. Alternatively, a laboratory estimate of 20% for the methane production yield would require a lifetime of 60 Earth yr.

*Unified Astronomy Thesaurus concepts:* Mars (1007); Meteoroids (1040); Meteors (1041); Meteorites (1038); Meteorite composition (1037); Comets (280); Asteroid belt (70); Long period comets (933); Methane (1042); Complex organic molecules (2256); Zodiacal cloud (1845); Short period comets (1452)

*Materials only available in the online version of record:* animations

## 1. Introduction

One of the main goals of recent Martian exploration is to understand and constrain the cycle of organic matter on the planet, along with searching for vestiges of either extinct or potentially existing life (Grady & Wright 2006). The Viking landers were the first missions able to detect the presence of carbon at the Martian surface in 1976, even though the results were somewhat contradictory: on the one hand, CO<sub>2</sub> release was detected via aqueous oxidation from samples of Martian soil (Levin & Straat 1979a, 1979b); on the other hand, gas chromatography/mass spectrometry experiments did not confirm the existence of any volatile organic compounds from heated samples, along with no by-product from pyrolysis of organic matter (Biemann et al. 1976). Similarly, the Thermal Evolved Gas Analyzer on board the Phoenix Mars lander (Hoffman et al. 2008) could not find evidence of organic fragments after heating samples to ~1300 K (Ming et al. 2009). Subsequently, the Sample Analysis at Mars (SAM) instrument on board the Mars Science Laboratory (MSL) Curiosity rover reported the identification of chlorobenzene and dichloroalkanes, which are likely the reaction products of Martian chlorine and organic carbon (Freissinet et al. 2015), at the Gale crater. Likewise, the SAM instrument was able to confirm for the first

time the presence of some unoxidized organic molecules, including thiophenic and aromatic compounds (Eigenbrode et al. 2018; ten Kate 2018).

One important question is the source and nature of organic carbon at the Martian surface. It has been proposed that the main supplier of organic species to the planetary surface is exogenous cosmic dust particles (i.e., interplanetary dust particles, IDPs) by 2 orders of magnitude over other possible sources (Chyba & Sagan 1992). In this regard, several studies have aimed to quantify the accretion rates of meteoric organic matter at the Martian surface. (1) Flynn (1996) estimated the global flux of intact carbon of 678 kg sol<sup>-1</sup> extrapolating from the flux at Earth and taking into account crater impacts in the Martian surface along with the dynamical evolution of particles close to Mars' orbit. (2) Frantseva et al. (2018) inferred for the first time a carbon flux on Mars from impacts of asteroids and comets of 177 kg sol<sup>-1</sup>, performing dynamical simulations of impact rates on Mars. (3) Carrillo-Sánchez et al. (2020b) also constrained the separate contribution of dust from asteroids and comets by using the zodiacal cloud model (Nesvorný et al. 2011), inferring a global accretion rate of organics at the Martian surface of only 14 kg sol<sup>-1</sup>. In addition, there are also indigenous mechanisms that might form organics: (1) in situ formation through water-rock interactions (Sharma et al. 2023) and (2) interactions among spinel-group minerals, sulfides, and a brine that facilitate the electrochemical reduction of aqueous CO<sub>2</sub> to organic molecules (Steele et al. 2018).

An important question is the fate of organic compounds at the surface of Mars. Benner et al. (2000) proposed that the



Original content from this work may be used under the terms of the [Creative Commons Attribution 4.0 licence](https://creativecommons.org/licenses/by/4.0/). Any further distribution of this work must maintain attribution to the author(s) and the title of the work, journal citation and DOI.

Martian regolith is likely oxidizing due to photolysis by UV radiation of H<sub>2</sub>O and subsequent OH and H radical chemistry producing peroxides and other oxidizing compounds. In this context, organic molecules would be mainly converted to carboxylic acids under oxidizing conditions with a production yield of benzoic acid of 10%. In summary, Benner et al. (2000) predicted that approximately 2 kg m<sup>-2</sup> of benzoic acid has been produced in the Martian soil during the last 3 Gyr, leading to an average concentration of ~500 ppm in the first meter of the surface. Apart from that, the detection of perchlorate salts at the Martian surface by the Phoenix lander mission (Hecht et al. 2009) and by the Curiosity rover (Glavin et al. 2013) suggests that perchlorates create an oxidizing environment within the regolith, giving rise to the disaggregation and destruction of organic molecules (Steininger et al. 2012; Carrier & Kounaves 2015; Crandall et al. 2017). Furthermore, Schuerger et al. (2011, 2012) and Keppler et al. (2012) showed from laboratory experiments that organic matter in meteorites at the Martian surface may be degraded by UV photolysis, resulting in the production of methane. It is likely that both oxidation by the presence of perchlorates and photolysis by UV irradiation contribute to degrade and remove available organic carbon from the Martian reservoir.

Methane was detected by tunable diode laser spectroscopy on the Mars Curiosity rover, with a mixing ratio of around 0.4 ppbv (Webster et al. 2015). There is some indication of an annual variation, from a minimum of ~0.2 ppbv at a solar longitude ( $L_s$ ) of 60° to a maximum of 0.6 ppbv at  $L_s = 160^\circ$  (Webster et al. 2018). Four potential sources were postulated to explain these observations (Atreya et al. 2007): (1) a volcanic source, although given that SO<sub>2</sub> has not been detected in the Martian atmosphere, this is quite unlikely; (2) hydrogeochemical processes involving serpentinization at temperatures below 420 K; (3) a biogenic source due to the presence of a microbial population in the subsurface of Mars; and (4) an exogenous source such as comets and asteroids. For the last case, Moores & Schuerger (2012) developed a model to determine the steady-state concentration of meteoric organic carbon at the surface of Mars if UV photolysis is the main removal mechanism (Schuerger et al. 2012), concluding that the background methane concentration due to UV photolysis of meteoric organic matter ranges from 2.2 to 11 ppbv. More recently, observations using the Nadir and Occultation for Mars Discover (NOMAD) spectrometer on board the ExoMars Trace Gas Orbiter (TGO) did not observe methane above the detection limit of 0.02 ppbv at altitudes higher than 20 km (Knutsen et al. 2021; Montmessin et al. 2021).

In this study, we explore the cycle of exogenous organic matter on Mars in the current geological period. For this purpose, we have developed a comprehensive model that describes (1) the entry of cosmic dust particles from the most relevant meteoroid populations in the inner solar system, (2) the pyrolysis of organic material in the upper atmosphere, (3) the accretion of intact carbon at the surface, and (4) the potential production of methane by UV photolysis.

## 2. Modeling the Seasonal and Latitudinal Distributions of the Accreted Meteoric Organic Matter at the Surface of Mars

Figure 1 is a diagram showing the variability with orbital position, defined by  $L_s$ , of the overall mass flux of deposited micrometeorites (MMs), including both unmelted

micrometeorites (uMMs) and cosmic spherules (CSs),<sup>5</sup> along with the total accreted mass of intact carbon and the methane production rates by UV (200–400 nm) radiation at the Martian regolith. This figure summarizes some of the results that are discussed in more detail in the following sections, and it completes the results depicted in Figure 1 in Carrillo-Sánchez et al. (2022). Figure 1 also shows the vertical distance of Mars (in au) relative to the ecliptic plane (highlighted in yellow) as a function of the orbital position.

### 2.1. A Dynamical Model of the Meteoroid Distribution: The Meteoroid Input Function for Mars

In this study, we will assess the dynamical evolution of the main meteoroid populations in the sporadic background around Mars' orbit with the meteoroid input function (MIF) model (Janhes et al. 2020), which has been recently used to characterize the deposition of meteor-ablated metals in the upper atmosphere of Mars, taking into account the temporal, vertical, latitudinal, and seasonal distribution (Carrillo-Sánchez et al. 2022). In summary, the MIF model for Mars uses the most recent version of the dynamical model of the zodiacal cloud (DMZC; Pokorný et al. 2017, 2018, 2021; Pokorný et al. 2019), which describes the dynamical evolution of bodies with diameters between 10 and 2000 μm of four meteoroid populations in the inner solar system around the sporadic background of Mars: the Jupiter-family comets (JFCs), the main-belt asteroids (ASTs), the Halley-type comets (HTCs), and the Oort Cloud comets (OCCs). As discussed in Carrillo-Sánchez et al. (2022), the DMZC does not consider the contribution of meteor showers in the inner solar system given that they may represent <10% of the overall number flux observed by radars at Earth (Brown et al. 2008). Additionally, the DMZC assumes that the contribution of meteoroids from the Edgeworth–Kuiper Belt (EKB) to the overall mass flux in the inner solar system within 5 au is negligible (Poppe 2016; Poppe et al. 2019). It should be noted, however, that a recent study suggests that bodies from the EKB in the inner solar system may exhibit an evolved dynamics with exposure ages >1 Myr (Keller & Flynn 2022), even though it is rather likely that the radiant and velocity distributions of these particles are fairly similar to those shown by the JFCs and the ASTs (Fraser et al. 2022). In the present study, we use the fitting procedure described in Carrillo-Sánchez et al. (2016, 2020b), which only considers the contribution to the total mass input of three meteoroid populations in the inner solar system: the JFCs, the ASTs, and the HTCs, where the HTCs represent all the long-period comets.

The DMZC provides high-resolution maps of the mass flux and the entry velocities for the four meteoroid populations as a function of ecliptic longitude and latitude (measured from the orbital plane of Mars). The MIF model allows the radiant distributions in ecliptic coordinates to be transformed into the

<sup>5</sup> Note that the uMMs represent all those bodies that do not reach the melting temperature necessary to commence atmospheric ablation (Vondrak et al. 2008; Carrillo-Sánchez et al. 2015). CSs refer to MMs that ablated partially after exceeding the threshold melting temperature. CSs are estimated to be CI- and CM-like fine-grained aggregates containing anhydrous and hydrated silicate minerals (Taylor et al. 1998). In this respect, hydrated silicates experience chemical and mineralogical reactions above ~900 K, whereas the melting points of anhydrous silicates span a range of temperatures between ~1400 and ~2200 K, constraining the ablation characteristics of the incident meteoroid influx (Greshake et al. 1998). In this study, we consider that the particle is fully melted above 1800 K (Vondrak et al. 2008; Gomez Martin et al. 2017).

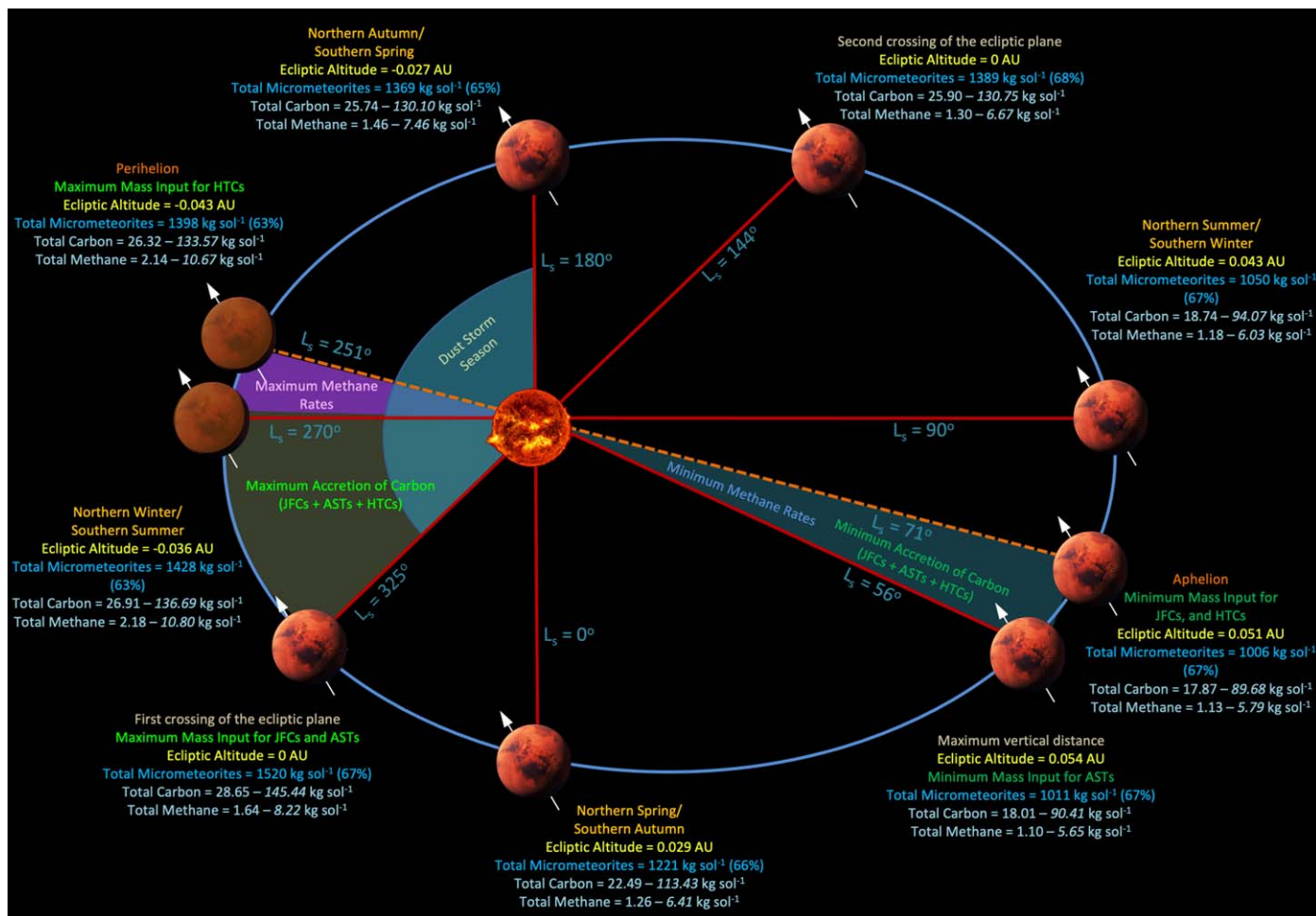


**Figure 1.** Diagram illustrating the variability with the orbital position ( $L_S$ ) of the total mass flux of MMs, the total accreted mass of carbon, and the methane production rates by UV (200–400 nm) radiation at the Martian surface. The values in parentheses represent the fraction of total MMs with respect to the total initial mass input before atmospheric ablation. The fluxes of carbon and the methane production rates are first estimated assuming a CI-chondrite carbon content of 5 wt% for all meteoroid populations, while the values in italics represent the corresponding fluxes for a carbon content of 25.6 wt% for comets—JFCs and HTC (see also Figure 4). The methane fluxes shown in this figure are calculated assuming a UV photolysis yield for methane production of 20%. As discussed in Section 2.3, the methane production rates are estimated considering the yearly average accretion rates of carbon and, therefore, assuming that the reservoir of carbon is not altered substantially by the orbital fluctuations of the accretion of MMs; therefore, the methane fluxes only depend on the latitudinal and orbital fluctuations of UV radiation at the Martian surface. The maximum accretion of MMs is located around the FCEP ( $L_S = 325^\circ$ ), whereas the maximum methane rates occur between  $L_S = 251^\circ$  (perihelion) and  $L_S = 270^\circ$  (northern winter/southern summer). Note that the mass fluxes are expressed in  $\text{kg sol}^{-1}$  (1 solar day at Mars is equivalent to 1.0275 Earth days).

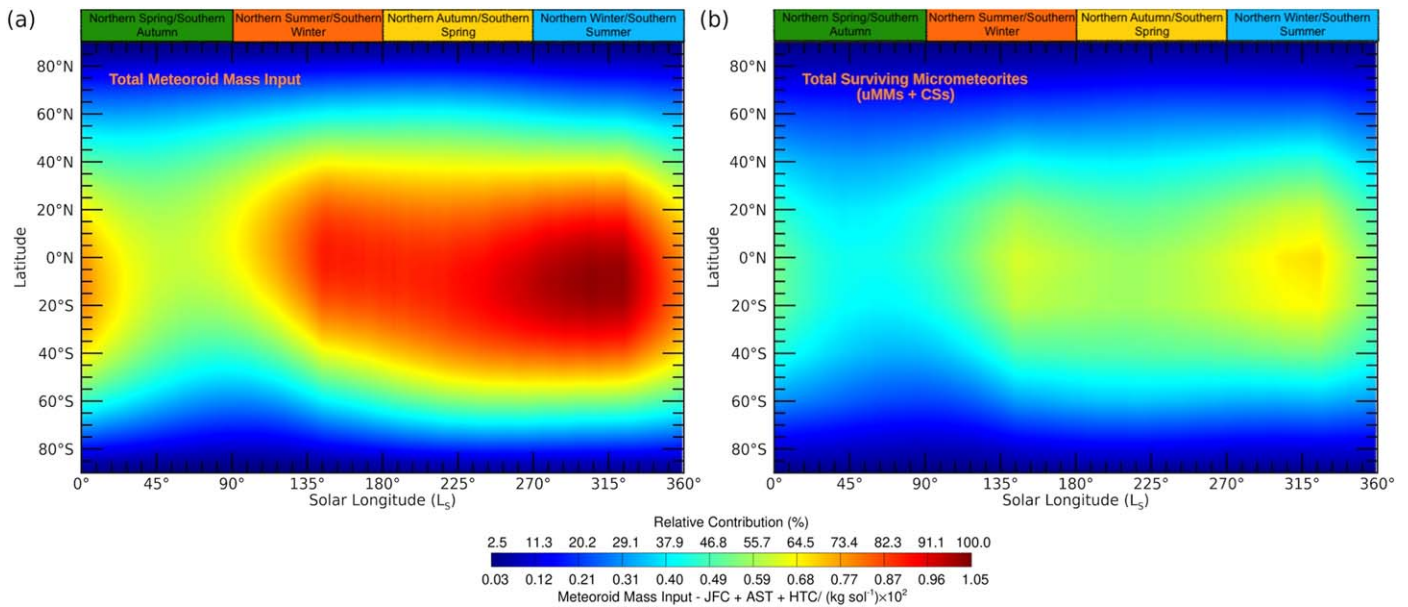
equivalent planetographic coordinates of a given planetary body (Janches et al. 2020). For this purpose, the MIF model estimates the elevation angle of the impinging particle—measured from the local horizon for an observer—from the corresponding ecliptic coordinates using the SPICE Toolkit<sup>6</sup> (Acton 1996; Janches et al. 2020) and assuming a planetographic grid with a fixed size bin  $\Delta\lambda = \Delta\phi = 5^\circ$ , where  $\lambda$  and  $\phi$  are the Martian longitude and latitude, respectively.

Figure 2(a) shows the seasonal variability of the total mass input of meteoroids estimated by the MIF model after adding the relative contributions of the JFCs, ASTs, and HTC before atmospheric entry in  $\text{kg sol}^{-1}$  and as a function of Martian latitude and  $L_S$ . Note that the overall mass fluxes in Figure 2 are not normalized with the corresponding surface area of each latitudinal band in order to highlight the differences of the mass input fluxes between the equator and the polar regions. According to Figure 2(a), most of the meteoroid contributions occur between the second crossing of the ecliptic plane (SCEP;

$L_S = 144^\circ$ ) and the first crossing of the ecliptic plane (FCEP;  $L_S = 325^\circ$ ). Additionally, the maximum total mass influx appears between northern winter ( $L_S = 270^\circ$ ) and the FCEP, peaking at  $L_S = 306^\circ$ , while the minimum mass influx occurs around aphelion ( $L_S = 71^\circ$ ).

The solid lines in Figure 3 show the average mass input over a Martian year as a function of entry velocity for the JFCs (blue), ASTs (green), HTC (orange), and total input (black). Figure 3 also shows the corresponding mass influxes between aphelion (dashed-dotted lines) and perihelion (dashed lines), illustrating how the velocity of the impacting meteoroids is modulated by the orbital velocity of Mars ( $v_{\text{orb}} = 21.2 \text{ km s}^{-1}$  at aphelion and  $v_{\text{orb}} = 26.5 \text{ km s}^{-1}$  at perihelion). There are several points to note. First, the JFCs are the main mass contributor to the overall mass influx for velocities below  $20 \text{ km s}^{-1}$  and have an annual average velocity of  $11.7 \text{ km s}^{-1}$ , that is, between an average velocity of  $11.1 \text{ km s}^{-1}$  at aphelion and  $12.3 \text{ km s}^{-1}$  at perihelion. Second, the HTC with an annual average velocity of  $27.2 \text{ km s}^{-1}$  are the dominant source for faster particles above  $20 \text{ km s}^{-1}$ , with typical velocities between  $25.5$  and  $28.8 \text{ km s}^{-1}$

<sup>6</sup> See <https://naif.jpl.nasa.gov>.



**Figure 2.** Seasonal and latitudinal variability of the overall mass influxes, in  $\text{kg sol}^{-1}$ , of meteoroids before atmospheric entry (panel (a)) and total accreted MMs at the Martian surface—uMMs and CSs (panel (b))—as a function of the Martian latitude and the solar longitude.

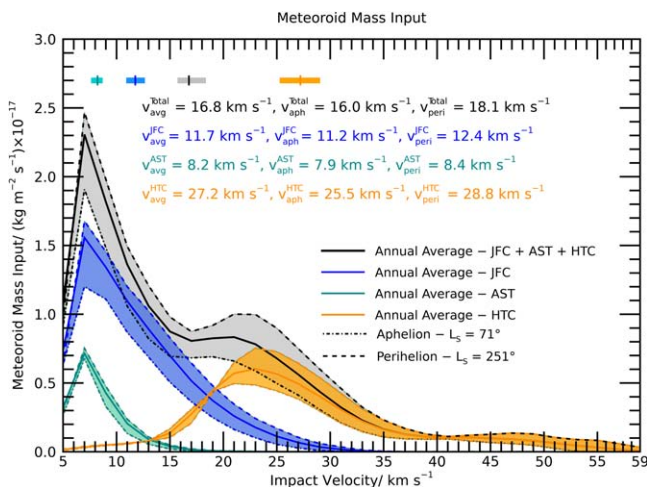


**Figure 3.** Annual average mass input as a function of the impact velocity for the JFCs (solid blue line), ASTs (solid green line), HTCs (solid orange line), and total mass flux (solid black line). The shaded regions represent the corresponding mass influxes between aphelion ( $L_S = 71^\circ$ ; dashed-dotted lines) and perihelion ( $L_S = 251^\circ$ ; dashed lines). This figure also shows the annual average input velocities for each meteoroid population along with the corresponding average values at aphelion and perihelion. The lower and upper limits of the top bars illustrate the average velocity at aphelion and perihelion for each meteoroid population and the total mass influx, respectively. The vertical lines in these bars show the corresponding annual average input velocity.

at aphelion and perihelion, respectively. In contrast, the ASTs exhibit a significantly lower contribution with annual average velocities of  $8.2\text{--}7.9 \text{ km s}^{-1}$  at aphelion and  $8.4 \text{ km s}^{-1}$  at perihelion, closer to the escape velocity of Mars. As a result, the MIF model predicts an annual average velocity of the total mass input of  $16.8 \text{ km s}^{-1}$ , between  $16.0 \text{ km s}^{-1}$  at aphelion and  $18.1 \text{ km s}^{-1}$  at perihelion. These orbital fluctuations of the impact velocity of meteoroids mainly alter the overall fluxes of ablated metals in the upper atmosphere and, additionally, the fluxes of pyrolyzed organics, with HTCs being the main contributor (see Carrillo-Sánchez et al. 2022 and Section 3.1

in this manuscript). In contrast, the total accretion rates of organics at the Martian surface are not affected by the orbital shifts of the meteoroid entry velocities. As discussed in detail below, the JFCs are the main contributor to the overall fluxes of uMMs and, therefore, to the total accretion rates of organics at the surface. In this respect, even though the ratio of CSs to uMMs may increase slightly for the JFCs going from aphelion to perihelion due to an increase in the average velocity (see Table 1), the overall ratio of accreted carbon to uMMs, which indicates the fraction of intact carbon within uMMs that survives pyrolysis, remains essentially constant with orbital position.

## 2.2. Modeling the Accretion Rates of Organics at the Martian Surface with the Chemical Ablation Model

Recently, Carrillo-Sánchez et al. (2022) combined the MIF model (Janiches et al. 2020) with the most recent version of the University of Leeds Chemical Ablation Model (CABMOD; see Vondrak et al. 2008 and Carrillo-Sánchez et al. 2020a, 2020b) to provide for the first time a complete description of the temporal, vertical, latitudinal, and seasonal variability for the injection rates of the main meteoric chemical elements that ablate in the upper atmosphere of Mars—Si, Mg, Fe, Al, Ca, Ti, P, Na, K, and Ni. In summary, the MIF model considers the initial diameters, entry angles, and entry velocities for the meteoroid distributions discussed here, assuming 346 orbital positions throughout the Martian year and a fixed planetographic resolution of  $\Delta\lambda = \Delta\phi = 5^\circ$  (Janiches et al. 2020), and the CABMOD model accounts for the corresponding atmospheric density profiles of 11 latitudes ( $\phi = -90^\circ, -80^\circ, -60^\circ, -40^\circ, -20^\circ, 0^\circ, 20^\circ, 40^\circ, 60^\circ, 80^\circ, \text{ and } 90^\circ$ ) and four orbital positions ( $L_S = 0^\circ, 90^\circ, 180^\circ, \text{ and } 270^\circ$ ) using the Mars Climate Database<sup>7</sup> (MCD; Lewis et al. 1999).

The CABMOD model takes into account three fundamental assumptions about the physical properties of the particle before the ablation process. (1) As a reference, the elemental abundances of the chemical compounds are defined by a CI-chondrite

<sup>7</sup> [https://www-Mars.lmd.jussieu.fr/mcd\\_python/](https://www-Mars.lmd.jussieu.fr/mcd_python/)

**Table 1**  
Global Mass Input from the Three Cosmic Dust Sources for Mars at Aphelion and Perihelion in  $\text{kg sol}^{-1}$

Mass Flux	JFCs ( $\text{kg sol}^{-1}$ )		ASTs ( $\text{kg sol}^{-1}$ )		HTCs ( $\text{kg sol}^{-1}$ )		Total ( $\text{kg sol}^{-1}$ )	
	Aphelion	Perihelion	Aphelion	Perihelion	Aphelion	Perihelion	Aphelion	Perihelion
Total input mass <sup>a</sup>	766.39	1144.45	191.89	251.58	546.35	839.23	1504.63	2235.26
Total MMs (uMMs + CSs)	704.97	1033.93	168.93	213.31	132.52	150.79	1006.42	1398.03
Total ablated	61.42	110.52	22.95	38.27	413.83	688.54	498.20	837.33
Total uMMs	679.03	976.05	139.42	176.84	44.87	49.55	863.32	1202.44
Total CSs	25.94	57.88	29.51	36.47	87.65	101.24	143.10	195.59
Accreted sulfur	8.35–24.42	12.45–36.40	1.07–3.13	1.39–4.06	0.18–0.52	0.29–0.85	9.60–28.07	14.13–41.31
Accreted carbon	15.55–85.82	23.19–127.99	1.99	2.59	0.33–1.82	0.54–2.98	17.87–89.68	26.32–133.57
Carbon (soluble)	5.94–32.78	8.85–48.84	0.70	0.88	0.11–0.61	0.18–0.99	6.75–34.09	9.91–50.71
Carbon (insoluble)	9.61–53.04	14.34–79.15	1.29	1.70	0.23–1.27	0.36–1.99	11.13–55.06	16.40–82.84
Carbon ( $T < 900 \text{ K}$ )	15.34–84.66	22.85–126.11	0.87	1.17	0.12–0.66	0.18–0.99	16.33–86.19	24.20–128.27
Production of $\text{CH}_4$	1.02–5.61	1.86–10.27	0.10	0.26	0.01–0.07	0.03–0.15	1.13–5.78	2.14–10.67
Ablated sulfur	10.81–31.61	16.16–47.27	3.73–10.90	4.90–14.33	13.48–39.42	20.69–60.50	28.02–81.93	41.75–122.10
Ablated carbon	20.05–110.66	29.98–165.47	6.92	9.10	25.05–138.26	38.44–212.16	52.02–255.84	77.52–386.73

**Notes.** At Mars, 1 solar day is equivalent to 1.0275 Earth days. Note that the overall fluxes of surviving MMs are partitioned between uMMs and CSs. Similarly, the global flux of accreted carbon is split into the soluble and insoluble phases, also showing the corresponding contribution from those particles that do not reach the pyrolysis temperature ( $\sim 900 \text{ K}$ ) during their atmospheric entry. The fluxes of carbon and methane are estimated assuming a chondritic carbon content of 5 wt% for all meteoroid populations, whereas the values in italics represent the corresponding rates for an average carbon content in cometary particles of 25.6 wt% (see Figure 4). Similarly, the fluxes of sulfur are estimated for both a typical carbonaceous chondrite composition (2.5 wt%, in italics) and a CI-chondrite composition (7 wt%).

<sup>a</sup> Total input mass of meteoroids before atmospheric ablation.

composition for all the chemical constituents (Lodders & Fegley 2011), assuming that impacting bodies are mineralogically and compositionally similar to the primitive nebular condensate (Taylor et al. 2012). (2) The initial mass of the particles is inferred assuming a spherical shape with a silicate bulk density for CI chondrites of  $1570 \text{ kg m}^{-3}$  (Flynn et al. 2018). (3) To ensure that particles remain isothermal during heating and ablation, CABMOD is restricted to treating particles with initial  $D \leq 1500 \mu\text{m}$  (Vondrak et al. 2008; Dawkins et al. 2023). For simplicity, a particle is assumed to be fully melted if its temperature exceeds  $1800 \text{ K}$  (Vondrak et al. 2008). CABMOD does not include the potential vesicle formation of hydrated particles, which would lead to a sudden expansion of around 70% in volume above the solidus temperature of  $1414 \text{ K}$ , resulting in a decrease of the bulk density, particle deceleration, and peak temperature (Genge 2017). Experimental measurements using the University of Leeds Meteoric Ablation Simulator-2 (MASI-2) indicate that particles preserve most of their initial carbon content up to  $\sim 900 \text{ K}$ , after which pyrolysis commences (see Figure 4 in Bones et al. 2022), that is, well below the solidus temperature at which sudden vesicle formation might take place. Therefore, in terms of modeling the pyrolysis of organics, the potential effect of vesicular “parachuting” should not be relevant.

Organic matter appears in different forms in carbonaceous chondrites, ranging from soluble and relatively volatile hydrocarbons (hereafter soluble organic matter, SOM) to refractory and insoluble macromolecular polycyclic hydrocarbon compounds similar to the kerogen found in oil shales (hereafter insoluble organic matter, IOM) (Kerridge 1983; Sephton & Botta 2008). More specifically, the IOM may represent up to 70% of the total organic matter in CI chondrites (Hayatsu et al. 1977; Hayatsu 1980). Previous studies reported the contribution from comets and/or carbonaceous asteroids of prebiotic organic matter to the primitive Earth, particularly amino acids and nucleic-acid bases, concluding that most of these chemical compounds cannot

survive temperatures essentially higher than  $\sim 900 \text{ K}$  (Anders 1989; Basiuk & Douda 1999). Consequently, all those meteoroids that do not reach the threshold pyrolysis temperature during their atmospheric entry are the main supplier of intact carbon to the Mars surface (Flynn 1996; Carrillo-Sánchez et al. 2020b).

The first goal of the present study is to provide an updated estimate of the accretion rates of carbon at the Martian regolith, introducing the pyrolysis kinetics during the ablation process within the CABMOD-MIF model. For this purpose, the CABMOD model has been updated with a semiempirical model able to characterize the atmospheric injection rates from both the SOM and IOM organic fractions as well as sulfur compounds (Bones et al. 2022). This kinetic model for pyrolysis was validated using the Leeds MASI-2 experimental setup for a range of temperatures between  $625$  and  $1300 \text{ K}$ . According to the mass-resolved gas analysis subjected to linear temperature ramps between  $293$  and  $1300 \text{ K}$ , the meteoric organic carbon and sulfur compounds pyrolyze to  $\text{CO}_2$  and  $\text{SO}_2$ , respectively, and the oxygen required for the conversion was shown to be internal to the particle, since the yield of  $\text{CO}_2$  and  $\text{SO}_2$  was independent of the  $\text{O}_2$  fugacity in the reactor chamber, even at fugacities well above those encountered during atmospheric ablation (Bones et al. 2022). Accordingly, several studies suggest that C is primarily oxidized within the particle, i.e., via reduction of  $\text{FeO}$  or  $\text{Fe}_2\text{O}_3$  (Genge & Grady 1998; Cordier et al. 2011). Additionally, it is likely that there is a slight contribution of  $\text{H}_2\text{S}$  evaporating directly from particles. The time-resolved pyrolysis model of organics proposed by Bones et al. (2022) is based on the evaporation model of Saleh et al. (2017) for the relatively volatile SOM and refractory IOM components, where the total fraction of organic carbon ablated,  $F_{\text{ab}}^{\text{C}}$  in  $\text{atoms s}^{-1}$ , is defined as

$$F_{\text{ab}}^{\text{C}} = f_{\text{SOM}}[1 - e^{-k_{\text{SOM}}t}] + f_{\text{IOM}}[1 - e^{-k_{\text{IOM}}t}], \quad (1)$$

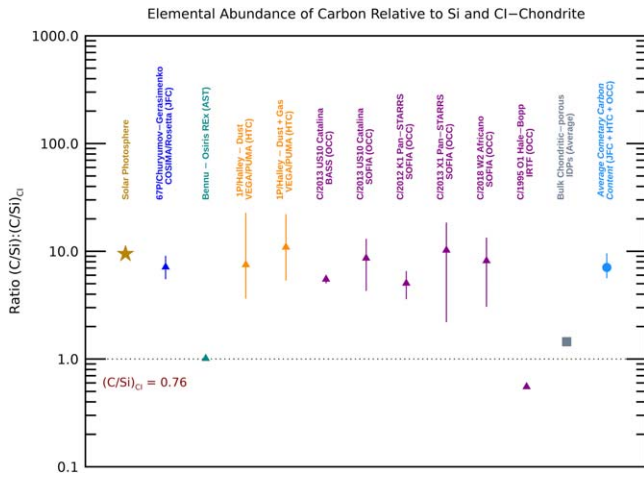


**Figure 4.** Elemental abundance of carbon relative to Si and to the CI-chondrite composition for the solar photosphere (brown star; Lodders & Fegley 2011) compared to the JFC 67P/Churyumov-Gerasimenko (blue triangle; Bardyn et al. 2017); the preliminary measurements of asteroid Benu by the OSIRIS-REx mission (dark cyan triangle; Witze 2023); the HTC 1P/Halley (orange triangles; Bergin et al. 2015); five OCCs, C/2013 US10 Catalina, C/2012 K1 Pan-STARRS, C/2013 X1 Pan-STARRS, C/2018 W2 Africano, and C/1995 O1 Hale-Bopp (magenta triangles; Woodward et al. 2021); and the average for bulk chondritic porous IDPs (gray square; Thomas et al. 1994). On average, cometary particles exhibit an enrichment in the elemental ratio of carbon relative to Si and to the CI-chondrite composition of  $7.1^{+2.4}_{-1.4}$  (light blue circle in Figure 4), leading to an average carbon content of 25.6 wt% for comets assuming a chondritic elemental abundance for the other chemical constituents. With regard to the sulfur content in meteoroids, compositional analysis indicates that bulk abundances of sulfur in typical carbonaceous chondrites are around 2–3 wt% (Court & Sephton 2011; Alexander et al. 2022), that is, exhibiting a depletion factor of  $\sim 2.9$  compared to a CI-chondritic composition. In the present study, we first consider a chondritic content of 5 wt% and 7 wt% to assess the accretion rates of carbon and sulfur, respectively, from particles with either cometary or asteroidal origin. However, the effect of both the carbon enrichment and sulfur depletion on the surface reservoir will be discussed in Section 3.

where  $f_{\text{SOM}}$  and  $f_{\text{IOM}}$  are the fraction of SOM and IOM in the particles, and  $k_{\text{SOM}}$  and  $k_{\text{IOM}}$  are the first-order rate constants for organic pyrolysis, respectively. Bones et al. (2022) fitted Equation (1) to get the best agreement between the modeled profiles and the experimental MASI-2 measurements assuming  $f_{\text{SOM}} = 0.59$  and  $f_{\text{IOM}} = 0.41$  for primitive meteorites (Hayes 1967). The resulting  $T$ -dependent rate coefficients  $k_{\text{SOM}}$  and  $k_{\text{IOM}}$  are

$$k_{\text{SOM}}[\text{in s}^{-1}] = \begin{cases} 1.2 \times 10^4 e^{-(7400/T)} & \text{where } T < 625 \text{ K;} \\ 2.5 e^{-(2100/T)} & \text{where } T \geq 625 \text{ K} \end{cases} \quad (2)$$

$$k_{\text{IOM}}[\text{in s}^{-1}] = \begin{cases} 1.1 \times 10^3 e^{-(7400/T)} & \text{where } T < 625 \text{ K;} \\ 2.9 e^{-(3700/T)} & \text{where } T \geq 625 \text{ K} \end{cases} \quad (3)$$

Similarly, the fraction of sulfur ablated,  $F_{\text{ab}}^{\text{S}}$  in atoms  $\text{s}^{-1}$ , can be calculated as

$$F_{\text{ab}}^{\text{S}} = \frac{\text{Swt\%/mw}_\text{S}}{\text{Cwt\%/mw}_\text{C}} F_{\text{ab}}^{\text{C}}, \quad (4)$$

where  $\text{mw}_\text{C}$  and  $\text{mw}_\text{S}$  are the molecular weight of carbon and sulfur, respectively. The carbon and sulfur content,  $\text{Cwt\%}$  and  $\text{Swt\%}$ , in primitive CI chondrites is 5 and 7 wt%, respectively (Lodders & Fegley 2011), although meteoroids may exhibit a relative enrichment or depletion of the elemental atomic abundances compared to primitive CI chondrites. In this way, the carbon content of IDPs may be around 10 wt% (Thomas et al. 1994) or even higher in those particles of recent cometary origin (Jessberger et al. 1988; Thomas et al. 1994; Altwegg et al. 2016). Figure 4 summarizes the elemental abundance of carbon relative to Si and the CI-chondrite composition for the solar photosphere (brown star; Lodders & Fegley 2011)

compared to the JFC 67P/Churyumov-Gerasimenko (blue triangle; Bardyn et al. 2017); the preliminary measurements of asteroid Benu by the OSIRIS-REx mission (dark cyan triangle; Witze 2023); the HTC 1P/Halley (orange triangles; Bergin et al. 2015); five OCCs, C/2013 US10 Catalina, C/2012 K1 Pan-STARRS, C/2013 X1 Pan-STARRS, C/2018 W2 Africano, and C/1995 O1 Hale-Bopp (magenta triangles; Woodward et al. 2021); and the average for bulk chondritic porous IDPs (gray square; Thomas et al. 1994). It should be noted that the preliminary analysis of some samples of asteroid Benu suggests that the carbon content is as much as 4.7 wt%, and the ratio shown in Figure 4 is estimated assuming a CI-chondritic composition for the other chemical constituents. In essence, Figure 4 reveals that most particles of cometary origin are significantly enriched in carbon compared to primitive CI chondrites, which have elemental abundances of C closer to the typical values of the solar photosphere, whereas the ASTs exhibit a CI-like ratio relative to Si for carbon of  $\sim 0.76$  (Lodders & Fegley 2011). On average, cometary particles exhibit an enrichment in the elemental ratio of carbon relative to Si and to the CI-chondrite composition of  $7.1^{+2.4}_{-1.4}$  (light blue circle in Figure 4), leading to an average carbon content of 25.6 wt% for comets assuming a chondritic elemental abundance for the other chemical constituents. With regard to the sulfur content in meteoroids, compositional analysis indicates that bulk abundances of sulfur in typical carbonaceous chondrites are around 2–3 wt% (Court & Sephton 2011; Alexander et al. 2022), that is, exhibiting a depletion factor of  $\sim 2.9$  compared to a CI-chondritic composition. In the present study, we first consider a chondritic content of 5 wt% and 7 wt% to assess the accretion rates of carbon and sulfur, respectively, from particles with either cometary or asteroidal origin. However, the effect of both the carbon enrichment and sulfur depletion on the surface reservoir will be discussed in Section 3.

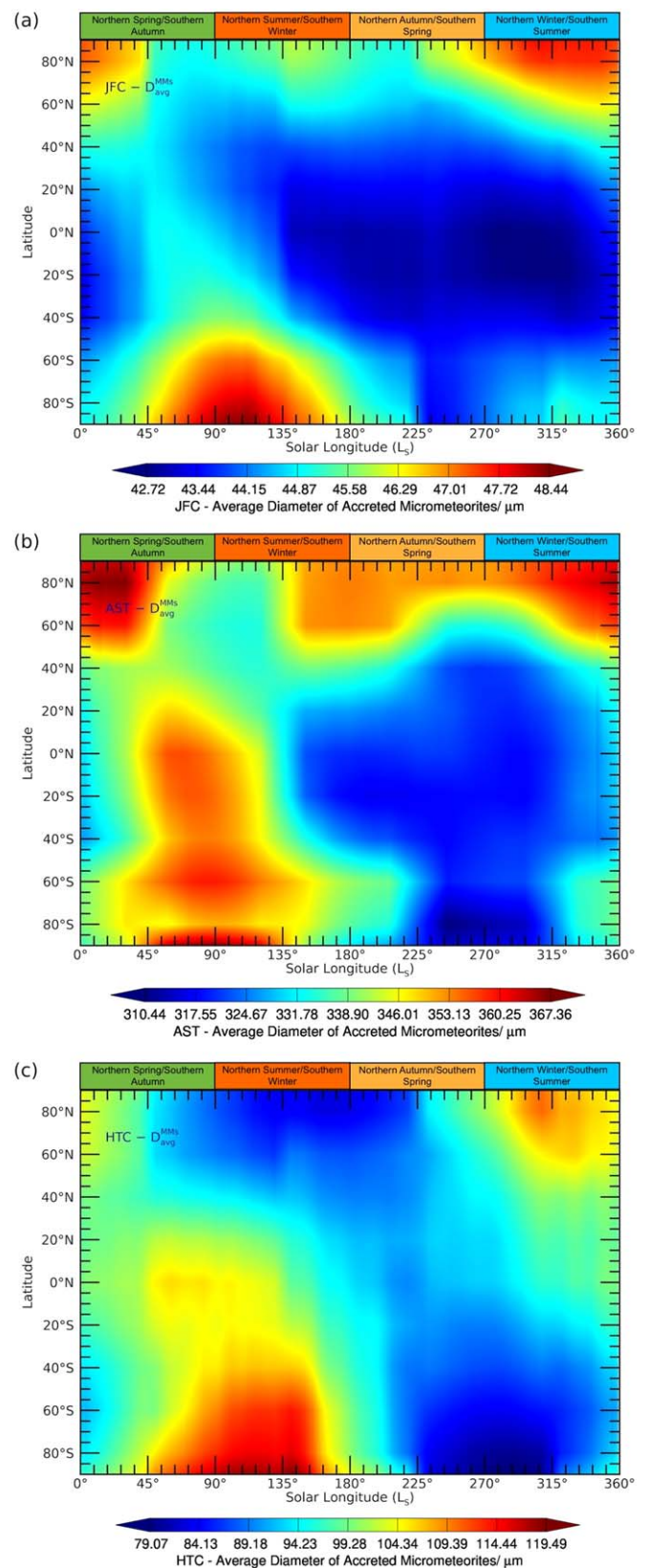
Figure 2(b) illustrates the seasonal and latitudinal variability of the total mass influxes of accreted MMs at the Martian surface in  $\text{kg sol}^{-1}$ , accounting for both the uMMs and CSs derived by the CABMOD-MIF model. For the CSs, we assume a bulk density of  $3200 \text{ kg m}^{-3}$  (Kohout et al. 2014). The color scale in Figure 2(b) is normalized to the maximum of the total mass influx of meteoroids before atmospheric ablation (see Figure 2(a)) to highlight the fraction of the initial mass input that reaches the Martian regolith. According to this figure, the total fluxes of MMs may represent up to 73% of the initial input around the FCEP at Mars' equator. In contrast, the combined effect of a nonzero inclination and an eccentric orbit leads to a significant decrease of both the mass influx of meteoroids (Figure 2(a)) and accreted MMs (Figure 2(b)) at aphelion (see Carrillo-Sánchez et al. 2022 for more details).

Carrillo-Sánchez et al. (2022) estimated the diurnal variability of the average diameter distribution for the three meteoroid populations before their atmospheric entry (see Figure 5 in Carrillo-Sánchez et al. 2022 for a detailed description). In this work, we have inferred the seasonal variability of the average diameter distributions, in microns, of the accreted MMs at the Martian surface as a function of latitude and  $L_S$  for the JFCs (Figure 5(a)), the ASTs (Figure 5(b)), and the HTCs (Figure 5(c)). In summary, the average size of the accreted MMs depends on the size and

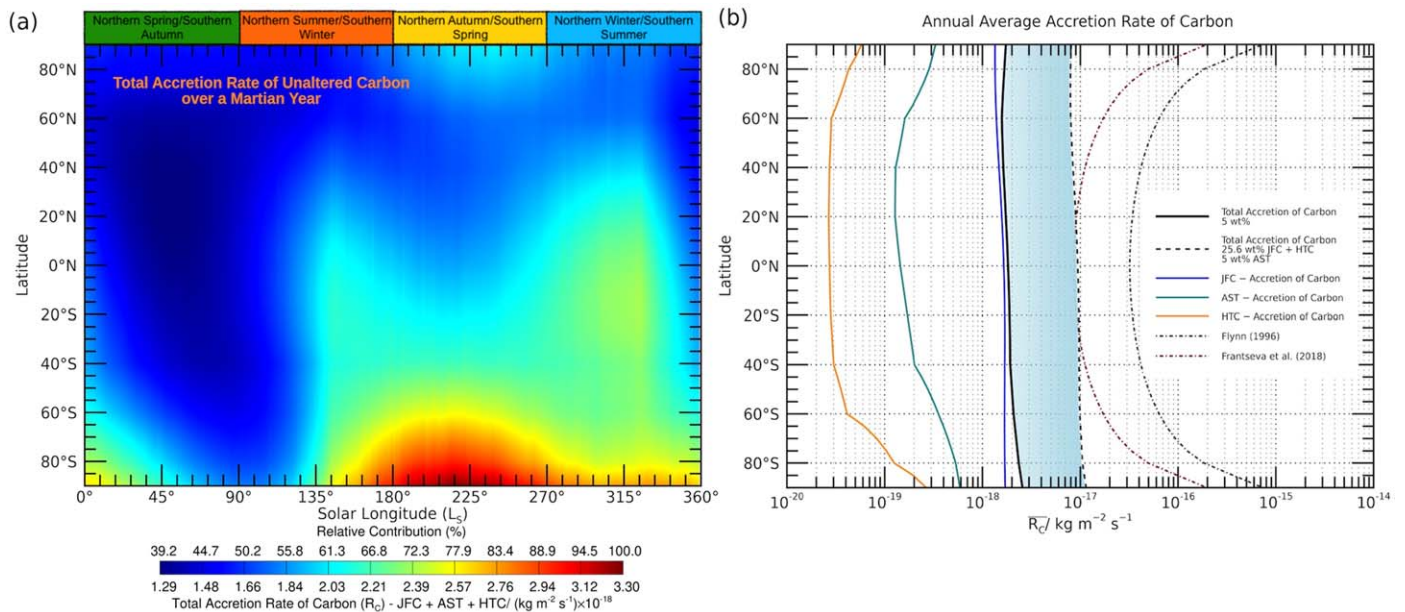
velocity distributions of the meteoroid populations before their atmospheric entry, characterized by the MIF model discussed in Section 2.1. For comparison, the MIF model predicts that JFCs are the main contributor to small particle sizes (Figures 5(a)–(c) in Carrillo-Sánchez et al. 2022) defined by slow bodies close to prograde orbits (blue lines in Figure 3), becoming the main contributor of accreted MMs at the Martian surface with average diameters in the narrow range of 42.7–48.4  $\mu\text{m}$  (Figure 5(a)). In contrast, the ASTs provide the initial largest particle sizes (Figures 5(d)–(f) in Carrillo-Sánchez et al. 2022) combined with velocities closer to the escape velocity of Mars (green lines in Figure 3), leading to the largest average diameters of accreted MMs in the broader range of 310.4–367.4  $\mu\text{m}$  (Figure 5(b)). In the case of the HTCs, the combination of comparatively large particle sizes (Figures 5(f)–(h) in Carrillo-Sánchez et al. 2022) with a faster velocity distribution (orange lines in Figure 3) provides average diameters for the deposited MMs between 79.0 and 119.5  $\mu\text{m}$  (Figure 5(c)).

Figure 5 also shows the latitudinal and seasonal variation of the average diameters of the accreted MMs for the three meteoroid populations as estimated by the CABMOD-MIF model. This figure indicates that the average particle sizes of the MMs increase to some extent at high latitudes around the northern/southern winter, because the axial tilt alters the latitudinal and seasonal distributions of both the entry velocity and the fraction of the particles with low elevation angles. On the one hand, the MIF model predicts that slower particles tend to be distributed at northern/southern high latitudes around the northern/southern winter (see Figure 6 in Carrillo-Sánchez et al. 2022), leading to an accretion of larger particles at these locations. On the other hand, the MIF model predicts that the relative contribution of the bodies entering closer to the local horizon increases substantially around the north pole during late northern winter and early northern spring and around the south pole between late southern fall and early southern winter. The CABMOD simulations show that meteoroids with initial low elevation angles penetrate deeper into the atmosphere without ablating significantly (see Table 4 in Vondrak et al. 2008), increasing the fraction of larger particles accreted at the surface. Interestingly, Moores et al. (2017) studied the possible redistribution of the deposited MMs across the Martian surface, assuming that MMs are mixed uniformly with surficial dust leading to the accumulation of MMs in regions of Mars with greater dust loading (Ruff & Christensen 2002). As a consequence, complete redistribution due to atmospheric dynamics close to the surface of Mars might significantly alter the seasonal and latitudinal size distribution of the accreted MMs shown in Figure 5; for example, the accumulation of larger MMs at the Martian polar regions during winter might be reduced. However, Ruff & Christensen (2002) considered dust particles with diameters of  $\sim 1 \mu\text{m}$ , that is, considerably smaller than the average diameters of MMs reported in the present study. Therefore, we do not treat the redistribution of deposited particles by winds at the Martian surface in this work.

Figure 6(a) presents the total accretion rates of carbon at the surface of Mars, in  $\text{kg m}^{-2} \text{s}^{-1}$ , as a function of the Martian latitude and the orbital position. Note that these fluxes are normalized with the corresponding surface area of each latitudinal band. For comparison, there is a marked increase



**Figure 5.** Seasonal and latitudinal variability of the average diameter distributions, in microns, of the accreted MMs at the Martian surface determined by the CABMOD-MIF model as a function of the Martian latitude and the solar longitude for the JFCs (a), the ASTs (b), and the HTCs (c). Note that the color scales are different for each meteoroid population.



**Figure 6.** Panel (a): total accretion rates of carbon at the surface of Mars, in  $\text{kg m}^{-2} \text{s}^{-1}$ , as a function of the Martian latitude and the solar longitude. Panel (b): annual average of the total accretion rates of carbon assuming an average carbon content of 5 wt% for all meteoroid populations, typical for CI chondrites (solid black line). The shaded blue region represents the accretion rates between a chondritic composition and those with a carbon content of 25.6 wt% for particles with a cometary origin (dashed black line). The contribution of each meteoroid population to the total accretion rates of carbon is also displayed in panel (b): the JFCs (solid blue line), the ASTs (solid green line), and the HTCs (solid orange line). Panel (b) also illustrates the fluxes of organic carbon inferred by Flynn (1996; dashed-dotted black line) and Frantseva et al. (2018; dashed-dotted red line) and weighted assuming the surface area of each latitudinal band has a resolution of  $5^\circ$ .

in the delivery of carbon at the surface between the SCEP ( $L_S = 144^\circ$ ) and the FCEP ( $L_S = 325^\circ$ ) due to the eccentricity of Mars' orbit, being mainly concentrated in the southern hemisphere because of the axial tilt, especially around the south pole during southern spring. Figure 6(b) shows the annual average of the total accretion rates of carbon assuming an average carbon content of 5 wt% for all meteoroid populations (solid black line). The shaded blue region represents the accretion rates between a chondritic composition and those with a carbon content of 25.6 wt% for particles with a cometary origin (dashed black line). The contribution of each meteoroid population to the total accretion rates of carbon is also displayed in Figure 6(b): the JFCs (solid blue line), the ASTs (solid green line), and the HTCs (solid orange line). For comparison, the deposition rates estimated by the CABMOD-MIF model are significantly lower than those derived by Flynn (1996; dashed-dotted black line) and Frantseva et al. (2018; dashed-dotted red line), weighted assuming the surface area of each latitudinal band has a resolution of  $5^\circ$ . It should be noted that the estimates derived by Flynn (1996) and Frantseva et al. (2018) correspond to a carbon content of 10 wt%, and these models treated the meteoroid mass and velocity distributions as uniform, both throughout Mars' orbit and latitudinally. As a result, as shown in Figure 6(b), the accretion rates of carbon estimated by Flynn (1996) and Frantseva et al. (2018) are markedly higher around the poles than in the equator after normalizing by the surface area of each latitudinal band, whereas the latitudinal and orbital fluctuations assumed by the CABMOD-MIF model attenuate these differences. As discussed above, the CABMOD-MIF model predicts that the JFCs are the main mass contributor to the overall flux of uMMs and, therefore, to the total flux of accreted carbon at the Martian regolith. The ASTs, and especially the HTCs, make a much smaller contribution. In comparison, as shown in Figures 5(b)

and (c), the ASTs and the HTCs may accrete MMs with larger average diameters at high latitudes during wintertime.

### 2.3. UV Degradation of Exogenous Organic Matter: Modeling the Potential Production of Methane from the Surface of Mars

The accretion rates of carbon at the Martian regolith, discussed in Section 2.2, create a surface reservoir that may be degraded by UV irradiation to yield methane (Moores et al. 2007; Schuerger et al. 2011, 2012; Keppler et al. 2012). Accordingly, Keppler et al. (2012) and Schuerger et al. (2012) reported the production of methane from carbonaceous chondrites exposed to UV radiation under simulated Martian conditions, concluding that even though methane generated by exogenous organic matter may explain a portion of the globally averaged methane abundance on Mars, it cannot describe the plume fluctuations of methane. Here we use the model of Moores et al. (2017) and Moores & Schuerger (2012) to quantify the production rate of methane, assuming several conditions about the physical properties and the specific history of the IDPs once they encounter the Martian atmosphere (see Section 3 in Moores & Schuerger 2012).

Moores & Schuerger (2012) considered that IDPs are CI- and CM-like fine-grained aggregates of submicron-sized particles containing anhydrous and hydrated silicate minerals (Brownlee 1985; Taylor et al. 1998), and each aggregate is surrounded by a rime of organics with a thickness between 50 and 200 nm. These rimes of organics create a glue-like matrix that binds the submicron silicate aggregates together (Flynn et al. 2003) and contain the carbon that may be degraded by UV photolysis. The model also assumes that once MMs are accreted at the Martian surface, UV photolysis will first degrade the outer rimes of carbon directly exposed to the radiation; the accreted particles then disaggregate over time,

allowing UV access to all the interior spaces (Schuerger et al. 2012).

Moore & Schuerger (2012) also assume that UV does not penetrate the interior of the IDPs while in interplanetary space, and that UV degradation of the organic matter only occurs at the Martian surface. Moore & Schuerger (2012) discussed two reasons why accreted MMs may be degraded faster under Martian surface conditions. First, exposure of organics to UV irradiation in interplanetary space may lead to the creation of a refractory layer that increases the resistance to UV penetration (Archer 2010). In this respect, a recent experimental study (Potapov et al. 2022) suggests the carbonization processes of molecular ices in the solar nebula that might have led to the formation of refractory materials through UV irradiation; consequently, the presence of molecular ices in the IDPs might produce a refractory structure around the particles, preserving organics from potential UV degradation. Furthermore, Moore & Schuerger (2012) proposed that these refractory layers would be removed before MMs are deposited at the Mars surface through either heating or detachment of the outer grains (i.e., fragmentation) during atmospheric entry, giving rise to fresh interior surfaces that can then be degraded by UV irradiation once the particles reach the Martian surface. However, there is experimental evidence indicating that cosmic dust particles become slightly harder after organic pyrolysis (Bones et al. 2022), so that they can withstand higher stresses that would prevent any fragmentation of the outer grains during atmospheric entry.

The second reason advanced to explain why UV degradation only occurs once MMs are accreted at the Martian surface is that the chemical conditions within the regolith are substantially different from interplanetary space, inducing the disaggregation of MMs. Moore & Schuerger (2012) suggested two chemical pathways that might be involved: (1) the presence of soil oxidants, such as perchlorates, which have been measured at the surface (Hecht et al. 2009; Glavin et al. 2013), degrade the organic matter (ten Kate et al. 2005; Schuerger et al. 2011, 2012); and (2) the presence of atomic hydrogen within the surface layer, produced by photochemistry immediately above the surface (Krasnopolsky 2006).

In order to model the UV degradation of organic matter under the Mars conditions, Schuerger et al. (2012) defined the quantum efficiency (QE), in  $\text{mol J}^{-1}$ , of the conversion of the surface organic carbon into methane as

$$\text{QE}(L_S, \phi) = 2.76 \times 10^{-10} F_{\text{CH}_4} [5.8 \times 10^{-4} (T_{\text{surf}}(L_S, \phi) - 273.15) + 0.126] [6.9 \chi_C + 0.026], \quad (5)$$

where  $F_{\text{CH}_4}$  is the methane flux in  $\text{nmol g}^{-1} \text{hr}^{-1}$ ,  $\chi_C$  is the mass fraction of carbon in the accreted MMs, and  $T_{\text{surf}}(L_S, \phi)$  is the temperature at the surface of Mars at a given latitude  $\phi$  and for a given orbital position  $L_S$ . In this study, we assumed the long-term rate of methane production reported by Schuerger et al. (2012),  $F_{\text{CH}_4} = 0.024 \text{ nmol g}^{-1} \text{hr}^{-1}$ . In the case of  $T_{\text{surf}}$ , we contemplate the seasonal and latitudinal variability of the diurnal average temperature at the Martian surface as provided by the MCD (see the left-hand panel of Figure 7(a)); this exhibits a minimum temperature of 141 K around the polar regions during winter and a maximum temperature of 249 K at high latitudes during southern summer due to the combined effect of a nonzero inclination and the eccentricity of Mars'

orbit. Likewise, as discussed in Section 2.2, one of the fundamental assumptions of CABMOD is that the elemental abundances of all chemical compounds are defined by a CI-chondrite composition (Lodders & Fegley 2011), so we assume a mass fraction of carbon of  $\chi_C = 0.05$  as the base case. The effect of carbon enrichment on particles from cometary origin is discussed in detail in Section 2.2.

The yearly average lifetime of accreted organics,  $L_n$ , in seconds, within the particle at a latitude  $\phi$  can be defined as the ratio between the total carbon content in the particle and the rate at which the carbon is depleted:

$$L_n(\phi) = \frac{2\chi_C \bar{f}_{P,n}(\phi) \bar{D}_n(\phi) \rho}{3\text{mw}_{\text{CH}_4} F_{\text{UV}}^{\text{avg}}(\phi) \text{QE}^{\text{avg}}(\phi)}, \quad (6)$$

where  $D_n$  is the diameter of a particle in the size bin  $n$  in meters,  $\rho$  is the silicate bulk density for CI chondrites of  $1570 \text{ kg m}^{-3}$  (Flynn et al. 2018),  $\text{mw}_{\text{CH}_4}$  is the molecular weight of methane ( $0.016 \text{ kg mol}^{-1}$ ),  $F_{\text{UV}}^{\text{avg}}(\phi)$  is the annual average UV flux in the range 200–400 nm at the Martian surface (see right-hand panel of Figure 7(b)),  $\text{QE}^{\text{avg}}(\phi)$  is the annual average QE calculated using the yearly average surface temperature (see right-hand panel of Figure 7(a)), and  $f_{P,n}$  represents the fraction of MMs that survive pyrolysis during atmospheric entry. Previous studies (Flynn 1996; Carrillo-Sánchez et al. 2020b) considered all those particles not heated above the organic pyrolysis temperature ( $\sim 900 \text{ K}$ ; Anders 1989) to estimate the fraction  $f_{P,n}$ ; however, in the present study,  $f_{P,n}$  is quantified using the empirical kinetic model for carbon pyrolysis discussed in Section 2.2. As discussed in Section 3.2, the typical lifetimes required to completely degrade the organic matter within a particle are considerably longer than a Martian year, so it is appropriate to use an average lifetime,  $L_n(\phi)$ , which only depends on latitude. Although the CABMOD-MIF model predicts, for the first time, the latitudinal and orbital variation of both the average size of the accreted MMs,  $D_n(L_S, \phi)$  (see Figure 5), and the fraction  $f_{P,n}(L_S, \phi)$ , here we consider the annual average of these quantities only accounting for the latitudinal variability, that is,  $\bar{D}_n(\phi)$  and  $\bar{f}_{P,n}(\phi)$ , respectively.

The total Mars surface loading of carbon,  $M_C$ , in  $\text{kg m}^{-2}$ , is expressed as

$$M_C(\phi) = \sum_n M_{C,n}(\phi) = \sum_n \bar{R}_{C,n}(\phi) L_n(\phi), \quad (7)$$

where  $\bar{R}_{C,n}(\phi)$ , in  $\text{kg m}^{-2} \text{s}^{-1}$ , is the annual average of the total accretion rate of carbon estimated by the CABMOD-MIF model at the surface for a size bin  $n$  at a given latitude  $\phi$  and for a given orbital position  $L_S$  (see Section 2.2 and Figure 6(b)), and  $M_{C,n}(\phi)$  is the mass of all particles in size bin  $n$  on the surface in  $\text{kg m}^{-2}$ . As mentioned in Section 2.2, the CABMOD-MIF model can determine the latitudinal and orbital shifts of  $R_{C,n}$  (see Figure 6(a)). However, in this study, we only account for the latitudinal variability of the yearly average accretion rates of carbon. First, we consider that the Martian regolith is well mixed with the surface carbon over a geological timescale, and, consequently, the reservoir of carbon is not altered substantially by the orbital fluctuations of  $R_C$  throughout a Martian year (Moore & Schuerger 2012). Second, as

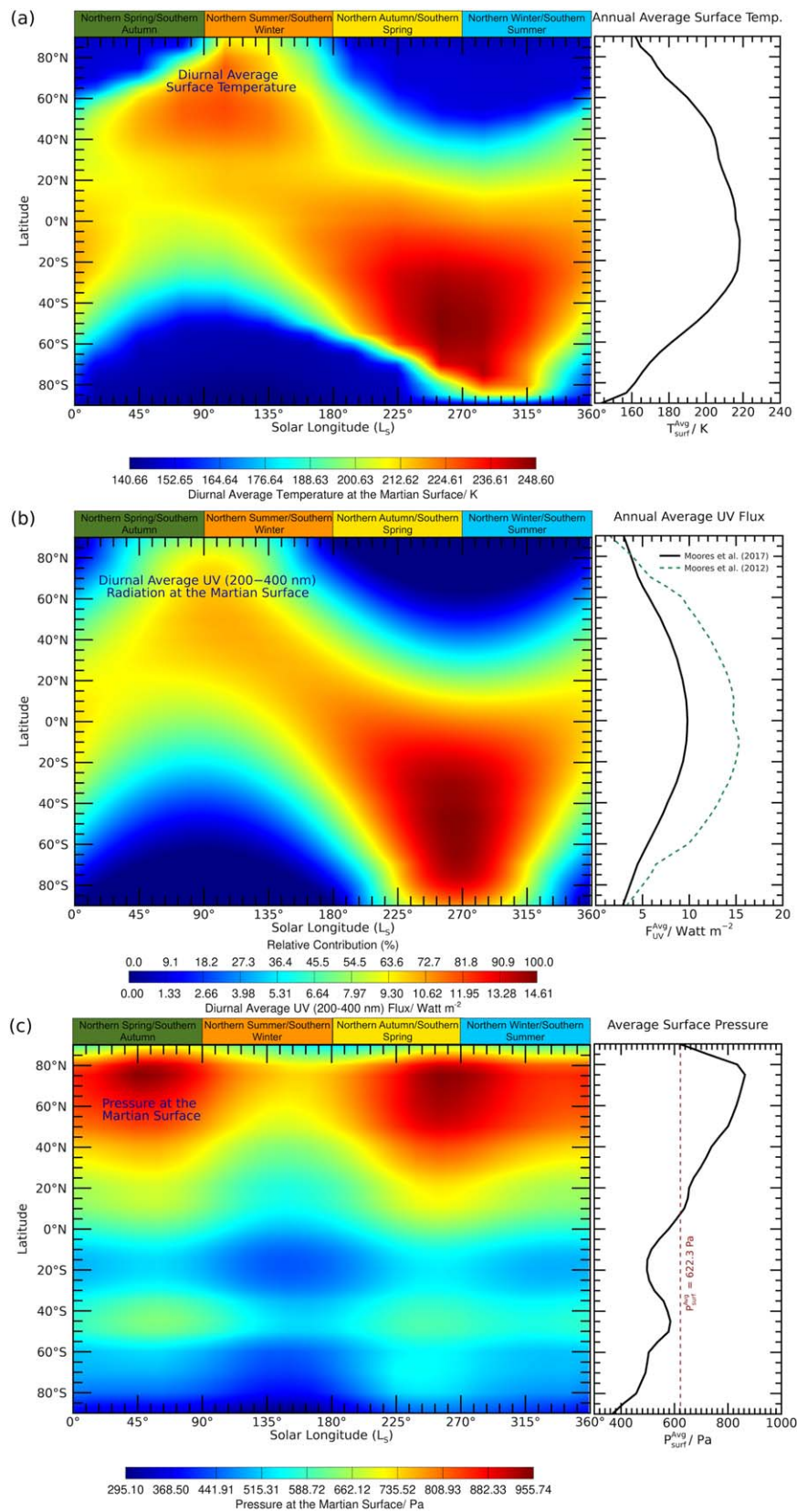


**Figure 7.** Seasonal and latitudinal variability for the diurnal average temperature at the Martian surface as provided by the MCD (left-hand panel of Figure 7(a)); the diurnal average UV radiation in the wavelength range between 200 and 400 nm, in  $W m^{-2}$ , at the surface of Mars (left-hand panel of Figure 7(b)); and the atmospheric pressure at the surface level provided by the MCD (left-hand panel of Figure 7(c)). Right-hand panels show the annual average surface temperature (Figure 7(a)), the annual average UV flux (solid black line; Moeres et al. 2017) compared to a previous estimate (dashed green line; Moeres & Schuerger 2012), and the annual average surface pressure (Figure 7(c)), where the vertical dashed red line represents the corresponding average value of this profile.

mentioned above, the required lifetime to fully degrade organics is essentially longer than a Martian year, and, therefore, UV photolysis of the surface load is not affected appreciably by orbital variations of the reservoir size of carbon.

Finally, the rate of methane production by UV radiation,  $N_{\text{CH}_4}(L_S, \phi)$ , in moles  $\text{m}^{-2} \text{s}^{-1}$  is

$$N_{\text{CH}_4}(L_S, \phi) = Y_{\text{CH}_4} \sum_n \frac{\bar{R}_{\text{C},n}(\phi) L_n(\phi) \bar{A}_n(\phi) F_{\text{UV}}(L_S, \phi) \text{QE}(L_S, \phi)}{\chi_{\text{C}} \bar{J}_{\text{P},n}(\phi) \bar{m}_n(\phi)}, \quad (8)$$

where  $\bar{A}_n(\phi)$  is the cross-sectional area of a single accreted particle at the Martian surface with a mass  $\bar{m}_n(\phi)$  in the size bin  $n$  at a given latitude  $\phi$ .  $F_{\text{UV}}(L_S, \phi)$  and  $\text{QE}(L_S, \phi)$  are the diurnal average UV radiation in the range 200–400 nm and the QE at the surface of Mars as a function of  $L_S$  and the Martian latitude  $\phi$ . Finally,  $Y_{\text{CH}_4}$  represents the reaction yield of the conversion of the surface organic carbon into methane, taken to be 0.2 (Schuerger et al. 2012).

The production rates of methane estimated by Equation (8) can then be converted into the equivalent column abundance  $c_{\text{CH}_4}$ , in ppbv  $\text{sol}^{-1}$ , assuming that  $N_{\text{CH}_4}$  is expressed as moles  $\text{m}^{-2} \text{sol}^{-1}$ , considering the atmospheric pressure at the Martian surface:

$$c_{\text{CH}_4}(L_S, \phi) = 10^9 \frac{N_{\text{CH}_4}(L_S, \phi)}{\left( \frac{P_{\text{surf}}}{g_{\text{Mars}} \text{mw}_{\text{CO}_2}} \right)}, \quad (9)$$

where  $P_{\text{surf}}$  is the surface pressure in Pa,  $g_{\text{Mars}}$  is the surface gravity of Mars ( $3.71 \text{ m s}^{-2}$ ), and  $\text{mw}_{\text{CO}_2}$  is the molecular weight of  $\text{CO}_2$  ( $0.044 \text{ kg mol}^{-1}$ ). According to the MCD, the atmospheric pressure at the surface level varies mainly with the latitude, exhibiting higher values in the northern hemisphere due to the generally lower orographic height at these latitudes (see left-hand panel in Figure 7(c)). For simplicity, in this study, we assume that the global abundance of  $\text{CH}_4$  is not altered by the changes of the surface pressure given its long lifetime in the atmosphere (Summers et al. 2002; Wong et al. 2003; Krasnopolsky et al. 2004; Atreya et al. 2007; see Section 3.3 for details), and, consequently, we consider that  $P_{\text{surf}} = 622.3 \text{ Pa}$  (see dashed red line in right-hand panel of Figure 7(c)). Therefore, we estimate that 1 ppbv of  $\text{CH}_4$  represents an atmospheric column abundance of  $3.80 \times 10^{-6} \text{ moles m}^{-2}$ .

Moores et al. (2017) and Moores & Schuerger (2012) developed a two-level radiative transfer model that includes both Rayleigh and Mie scattering and molecular absorption from a variety of atmospheric compounds (Tomasko et al. 1999) to characterize the yearly average of the UV irradiance at the Martian surface in the wavelength range 200–400 nm,  $F_{\text{UV}}^{\text{avg}}(\phi)$ ; see Equation (6). The latitudinal variability of  $F_{\text{UV}}^{\text{avg}}(\phi)$  estimated by Moores & Schuerger (2012) is represented by the dashed green line in the right-hand panel of Figure 7(b). This model has been subsequently refined and validated by Moores et al. (2017) using UV measurements on the surface of Mars by the Rover Environmental Monitoring Station instrument on board the MSL, as represented by the solid black line in the right-hand panel of Figure 7(b). In the present study, we estimate the UV radiance as a function of both latitude and

orbital position,  $F_{\text{UV}}(L_S, \phi)$ , in Equation (8); for this purpose, we have first modeled the total insolation flux at the Mars surface (Duffie & Beckman 2013), and this flux is then scaled in order to reproduce the average UV irradiance  $F_{\text{UV}}^{\text{avg}}(\phi)$  provided by Moores et al. (2017). The left-hand panel of Figure 7(b) represents the seasonal variation of the diurnal average UV flux, and the values are consistent with those reported by Patel et al. (2004) at the Martian surface. As expected, the total insolation at summertime southern latitudes increases markedly compared to the summertime northern region due to the eccentricity of Mars' orbit (see Figure 1).

### 3. Results and Discussion

#### 3.1. The Peak Altitude of Organic Pyrolysis as a Function of Latitude and Season

As discussed in Section 2.2, in this work, we assume that the exogenous organic matter that pyrolyzes during atmospheric ablation only produces  $\text{CO}_2$ , although it is quite likely that there are minor contributions from other carbon-containing species such as  $\text{CO}$ ,  $\text{C}_3\text{H}_8$ ,  $\text{C}_2\text{H}_4\text{O}$ , and  $\text{C}_2\text{H}_4$  (see Section 2.3 and Figure 2 in Bones et al. 2022). Indeed, a recent study suggests that a further fraction of organics may ablate as complex molecules that are not fully destroyed during atmospheric entry (DeLuca et al. 2022), indicating that compounds such as glycine may survive the ablation process (Glavin & Bada 2001; Jenniskens 2001). Nevertheless, according to Genge & Grady (1998) and Cordier et al. (2011), C is primarily oxidized within the particle via reduction of  $\text{FeO}$  or  $\text{Fe}_2\text{O}_3$ , which provide the oxygen required for pyrolysis reaction internal to the particle (Bones et al. 2022).

Carrillo-Sánchez et al. (2022) studied the combined effect of the orbital elements of Mars—the axial tilt or obliquity, the orbital eccentricity, and the inclination of the orbit to the ecliptic plane—on the altitude profiles of ablated meteoric compounds at different latitudes and orbital positions. Figure 8 summarizes the average diurnal variability of the total injection rate of  $\text{CO}_2$  (in molecules  $\text{m}^{-3} \text{s}^{-1}$ ) as a function of altitude and Local True Solar Time estimated by the CABMOD-MIF model at northern high latitudes ( $65^\circ < \phi < 90^\circ$ ; Figures 8(a), (f), (k), and (p)), northern midlatitudes ( $15^\circ < \phi < 65^\circ$ ; Figures 8(b), (g), (l), and (q)), equatorial latitudes ( $-15^\circ < \phi < 15^\circ$ ; Figures 8(c), (h), (m), and (r)), southern midlatitudes ( $-15^\circ < \phi < -65^\circ$ ; Figures 8(d), (i), (n), and (s)), and southern high latitudes ( $-65^\circ < \phi < -90^\circ$ ; Figures 8(e), (j), (o), and (t)). The columns in Figure 8 show the seasonal changes in the average injection rates of  $\text{CO}_2$ : northern spring/southern fall (left-hand panels, Figures 8(a)–(e)), northern summer/southern winter (panels in second column, Figures 8(f)–(j)), northern fall/southern spring (panels in third column, Figures 8(k)–(o)), and northern winter/southern summer (right-hand panels, Figures 8(p)–(t)).

Figure 8 shows that the  $\text{CO}_2$  injection rate peaks at equatorial latitudes between northern fall/southern spring and northern winter/southern summer (Figures 8(m) and (r)), with a marked midnight-to-noon enhancement. In contrast, the minimum deposition rates of ablated organics occur at northern/southern winter at high latitudes (Figures 8(j) and (p)) with typical values around 40% of the maximum injection rates of  $\text{CO}_2$ . Compared with the average diurnal variability of the total injection rates of the main meteoric constituents (see Figure 14 in Carrillo-Sánchez et al. 2022 for Mg), organics mostly ablate

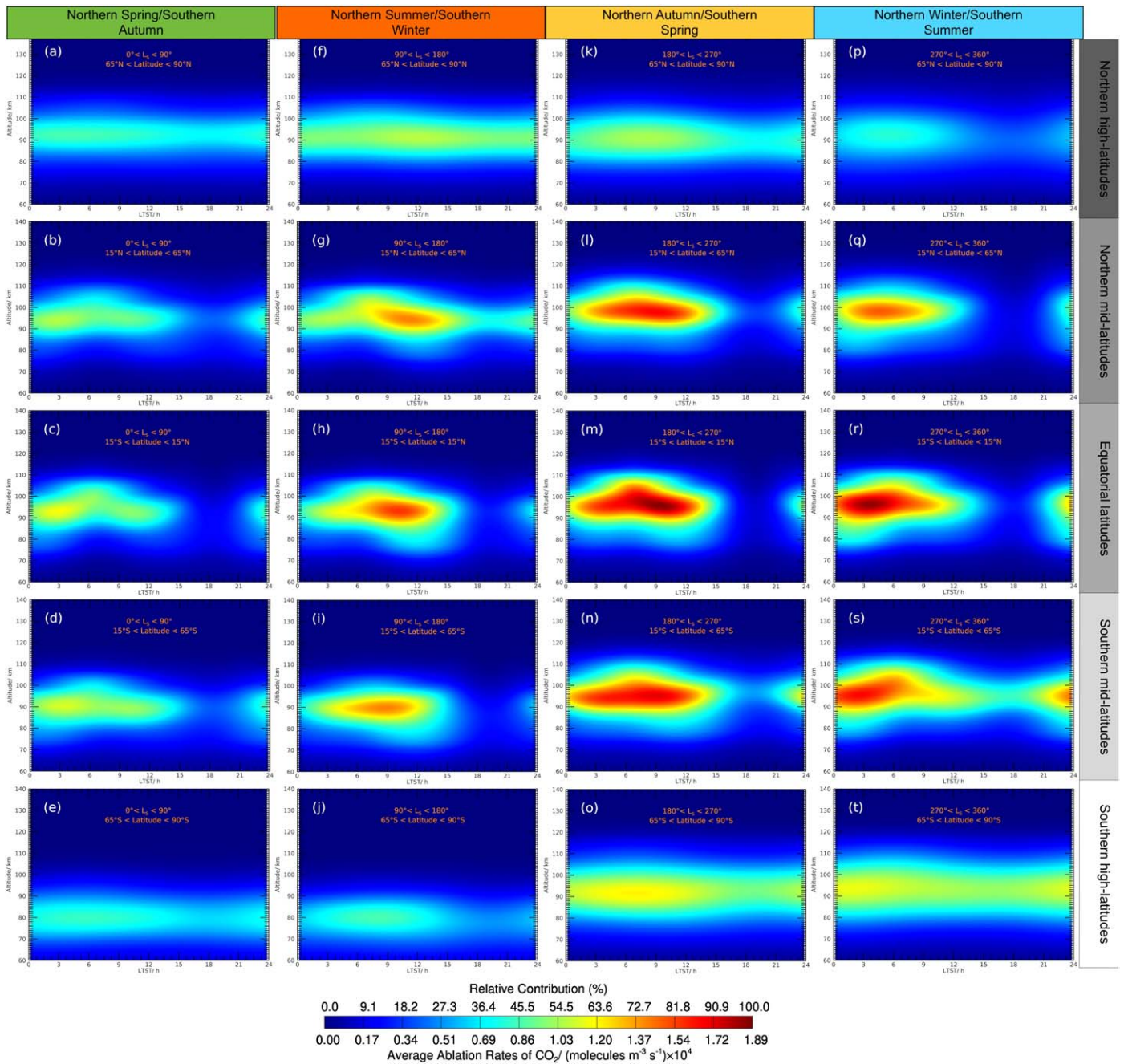


**Figure 8.** Average diurnal variability of the total injection rates, in molecules  $\text{m}^{-3} \text{s}^{-1}$ , of ablated  $\text{CO}_2$  estimated by the CABMOD-MIF model, assuming a chondritic carbon content of 5 wt% for all meteoroid populations, at northern high latitudes ( $65^\circ < \phi < 90^\circ$ ; panels (a), (f), (k), and (p)), northern midlatitudes ( $15^\circ < \phi < 65^\circ$ ; panels (b), (g), (l), and (q)), equatorial latitudes ( $-15^\circ < \phi < 15^\circ$ ; panels (c), (h), (m), and (r)), southern midlatitudes ( $-15^\circ < \phi < -65^\circ$ ; panels (d), (i), (n), and (s)), and southern high latitudes ( $-65^\circ < \phi < -90^\circ$ ; panels (e), (j), (o), and (t)). Left-hand panels represent the average rates between  $L_S = 0^\circ$  (northern spring/southern fall) and  $L_S = 90^\circ$  (northern summer/southern winter), panels in the second column show the average rates between  $L_S = 90^\circ$  (northern summer/southern winter) and  $L_S = 180^\circ$  (northern fall/southern spring), panels in the third column represent the average rates between  $L_S = 180^\circ$  (northern fall/southern spring) and  $L_S = 270^\circ$  (northern winter/southern summer), and right-hand panels show the average rates between  $L_S = 270^\circ$  (northern winter/southern summer) and  $L_S = 360^\circ$  (northern spring/southern fall). An animation of the ablation rates of  $\text{CO}_2$  at the equator (panels (c), (h), (m), and (r)) is available; the animation cycles through all solar longitudes, starting from aphelion  $L_S = 71^\circ$ , going to  $L_S = 0^\circ$ , and then to  $L_S = 71^\circ$ .

(An animation of this figure is available in the [online article](#).)

about 15 km higher irrespective of  $L_S$ , at similar heights as the alkali elements Na and K (see Figure 13 in Carrillo-Sánchez et al. 2022). Pyrolysis of organic carbon is complete before a dust particle fully melts at around 1800 K, corresponding to an atmospheric pressure level of  $\sim 0.01$  Pa (see Figure 16(a) in Carrillo-Sánchez et al. 2022). It is noteworthy that in CABMOD, the phase transition from the carbonaceous-

chondritic solid solution to the molten state is treated by applying a sigmoid temperature dependence centered at 1800 K with a width of 51 K (Gomez Martin et al. 2017; Bones et al. 2019).

With respect to the orbital elements of Mars (see also Section 3.3 in Carrillo-Sánchez et al. 2022), Figure 8 also shows that the obliquity leads to a northward/southward motion at a given

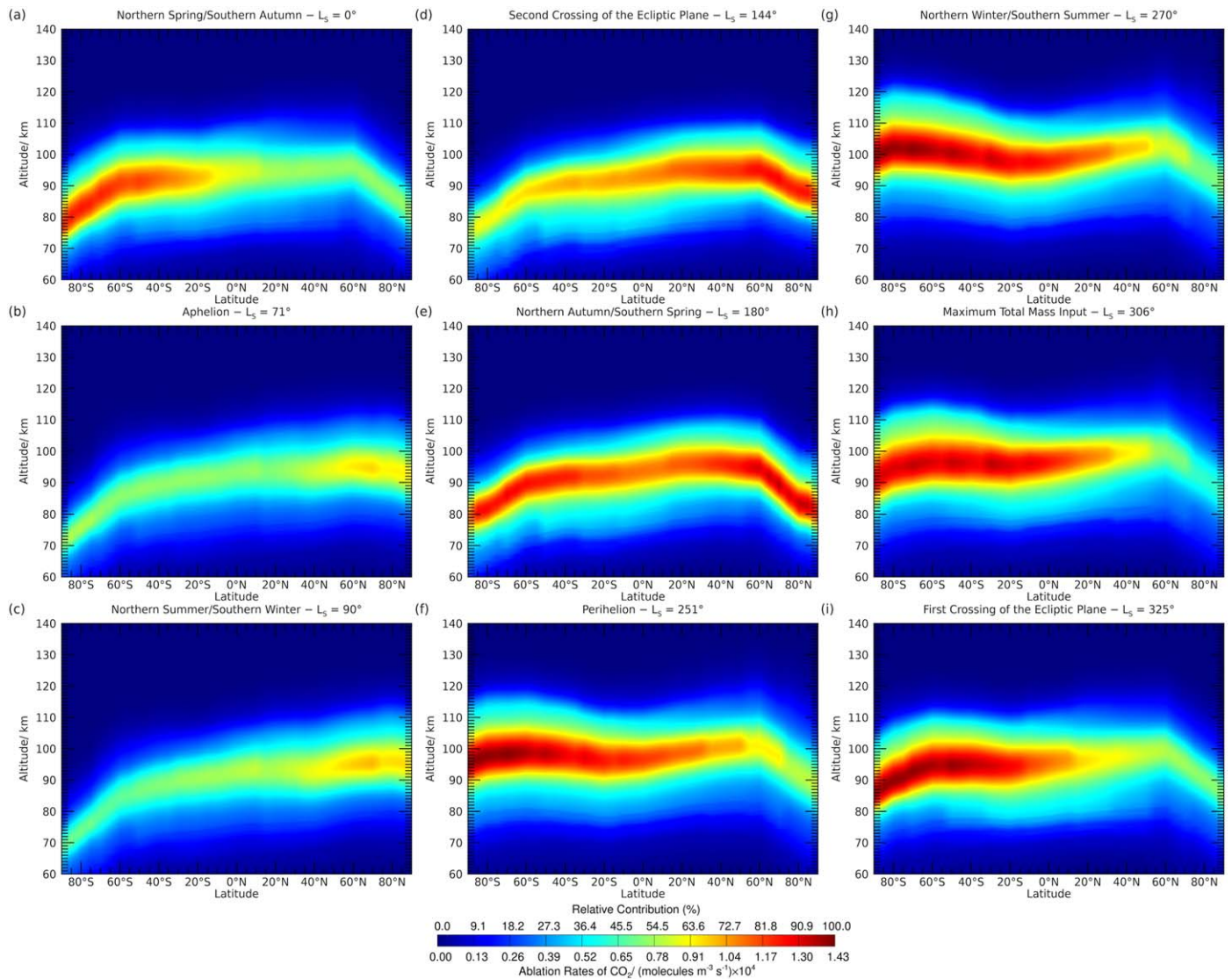


**Figure 9.** Seasonal variability of the total injection rates (in molecules  $\text{m}^{-3} \text{s}^{-1}$ ) of ablated  $\text{CO}_2$  estimated by the CABMOD-MIF model assuming a chondritic carbon content of 5 wt% for all meteoroid populations and weighted over a Martian day as a function of the height (in km) and the Martian latitude for the most relevant orbital positions:  $L_S = 0^\circ$  (panel (a); northern spring/southern fall),  $L_S = 71^\circ$  (panel (b); aphelion),  $L_S = 90^\circ$  (panel (c); northern summer/southern winter),  $L_S = 144^\circ$  (panel (d); SCEP),  $L_S = 180^\circ$  (panel (e); northern fall/southern spring),  $L_S = 251^\circ$  (panel (f); perihelion),  $L_S = 270^\circ$  (panel (g); northern winter/southern summer),  $L_S = 306^\circ$  (panel (h); maximum total mass input), and  $L_S = 325^\circ$  (panel (i); FCEP). An animation of the ablation rates of  $\text{CO}_2$  as a function of altitude and latitude is available; the animation cycles through all solar longitudes, starting from aphelion  $L_S = 71^\circ$ , going to  $L_S = 0^\circ$ , and then to  $L_S = 71^\circ$ .

(An animation of this figure is available in the [online article](#).)

$L_S$  of the peak  $\text{CO}_2$  ablation altitude, along with an attenuation of the midnight-to-noon distribution at mid- and high latitudes during northern/southern summer (Figures 8(f), (g), (s), and (t)) and at high latitudes during the northern/southern spring (Figures 8(a) and (o)). In addition, the combined effect of the eccentricity and the nonzero inclination of Mars' orbit gives rise to changes over a Martian year and at a given latitudinal band of the midnight-to-noon enhancement, the altitude of the ablation peak, and the magnitude of the ablated chemical species. For example, these fluctuations of the injection rates of  $\text{CO}_2$  can be visualized at northern high latitudes (Figures 8(a), (f), (k), and (p)), equatorial latitudes (Figures 8(c), (h), (m), and (r)), or southern high latitudes (Figures 8(e), (j), (o), and (t)).

Figure 9 shows the seasonal variability of the total  $\text{CO}_2$  injection rates as a function of the height and the latitude and weighted over a Martian day for the most relevant orbital positions:  $L_S = 0^\circ$  (panel (a); northern spring/southern fall),

$L_S = 71^\circ$  (panel (b); aphelion),  $L_S = 90^\circ$  (panel (c); northern summer/southern winter),  $L_S = 144^\circ$  (panel (d); SCEP),  $L_S = 180^\circ$  (panel (e); northern fall/southern spring),  $L_S = 251^\circ$  (panel (f); perihelion),  $L_S = 270^\circ$  (panel (g); northern winter/southern summer),  $L_S = 306^\circ$  (panel (h); maximum total mass input), and  $L_S = 325^\circ$  (panel (i); FCEP). As reported for the most relevant meteoric metals (see also Figure 15 in Carrillo-Sánchez et al. 2022 for Mg), the ablation heights of injected meteoric components shift markedly at high latitudes as Mars moves toward or away from northern/southern solstices: the injection of  $\text{CO}_2$  is up to 20 km lower at high winter latitudes than in the equatorial region. This is because the colder the atmospheric temperature profile, the deeper the penetration of the particle into the vertically contracted atmosphere before ablation starts. Moreover, similar to other meteoric species, the maximum injections of  $\text{CO}_2$  occur in southern mid- and high latitudes during perihelion and southern

summer (Figures 9(f) and (g)), but interestingly, there is a further marked peak in the abundance of CO<sub>2</sub> at southern mid- and high latitudes around the FCEP (Figure 9(i)), because this is when the maximum mass input for the JFCs occurs. Therefore, while the CABMOD-MIF model predicts that most ablated atoms are produced by HTCs, which are characterized by a high momentum and have a maximum injection around perihelion (Carrillo-Sánchez et al. 2022), those meteoroid sources mainly populated by slow-speed bodies, such as the JFCs, are a significant fraction of the total ablated organic matter with a maximum mass input around the FCEP (see also Section 3.2).

### 3.2. The Accretion Rates of Organic Matter at the Mars Surface

Table 1 lists the overall mass input fluxes for the three meteoroid populations before ablation, in kg sol<sup>-1</sup>, at aphelion and perihelion and the corresponding partitioning of the total input into total surviving MMs (uMMs + CSs) and total ablated mass. Similarly, the global flux of accreted carbon is split into the SOM and IOM fractions, also showing the accretion of carbon from those particles that do not reach the pyrolysis temperature (~900 K) during their atmospheric passage. The values in italics represent the corresponding rates assuming an average carbon content in cometary particles of 25.6 wt% and a sulfur content of 2.5 wt% for all meteoroid sources (see Section 2.2 and Figure 4). In summary, the contributions of the JFCs, the ASTs, and the HTCs to the total mass input are around 51%, 12%, and 37%, respectively, and they remain essentially constant between aphelion and perihelion. The global mass input ranges from  $1.5 \times 10^3$  to  $2.2 \times 10^3$  kg sol<sup>-1</sup> between aphelion and perihelion with an increase of around 50%, that is, within the broad mass range provided by the Langmuir Probe and Waves (LPW) instrument on board the Mars Atmosphere and Volatile Evolution (MAVEN) spacecraft of  $88\text{--}8.8 \times 10^3$  kg sol<sup>-1</sup> in the diameter range 2–24 μm (Andersson et al. 2015); however, note that the CABMOD-MIF model only predicts a total mass input of 110–160 kg sol<sup>-1</sup> in this narrow size range, closer to the lower limit of the mass input inferred by the MAVEN/LPW. Likewise, there is a decrease of the flux of MMs between aphelion and perihelion, representing 67% and 63% of the initial input, respectively, as a result of relatively faster particles at perihelion that ablate more efficiently (see Section 2.1). In summary, the JFCs are the main provider to the total mass influx of accreted uMMs with 679 and 976 kg sol<sup>-1</sup> at aphelion and perihelion, respectively, which represents between 67% and 70% of the deposited MMs at the Mars surface. In contrast, most of the deposited CSs are supplied by the HTCs with 88 and 101 kg sol<sup>-1</sup> at aphelion and perihelion, respectively, even though the overall CS/uMM ratio of 0.16 is practically constant regardless of the orbital position.

The pyrolysis kinetics module in the CABMOD-MIF model predicts that the pyrolysis efficiency of both organics and sulfur is ~74% with global injection rates between 52 and 78 kg sol<sup>-1</sup> of ablated carbon and 82 and 122 kg sol<sup>-1</sup> of sulfur at aphelion and perihelion, respectively, considering a CI-chondritic composition for all meteoroid populations. Assuming an average carbon content in cometary particles of 25.6 wt%, the injection rates of carbon range from 256 to 387 kg sol<sup>-1</sup> at aphelion and perihelion, respectively. Similarly, the overall flux of sulfur varies between 28 and 42 kg sol<sup>-1</sup> considering an

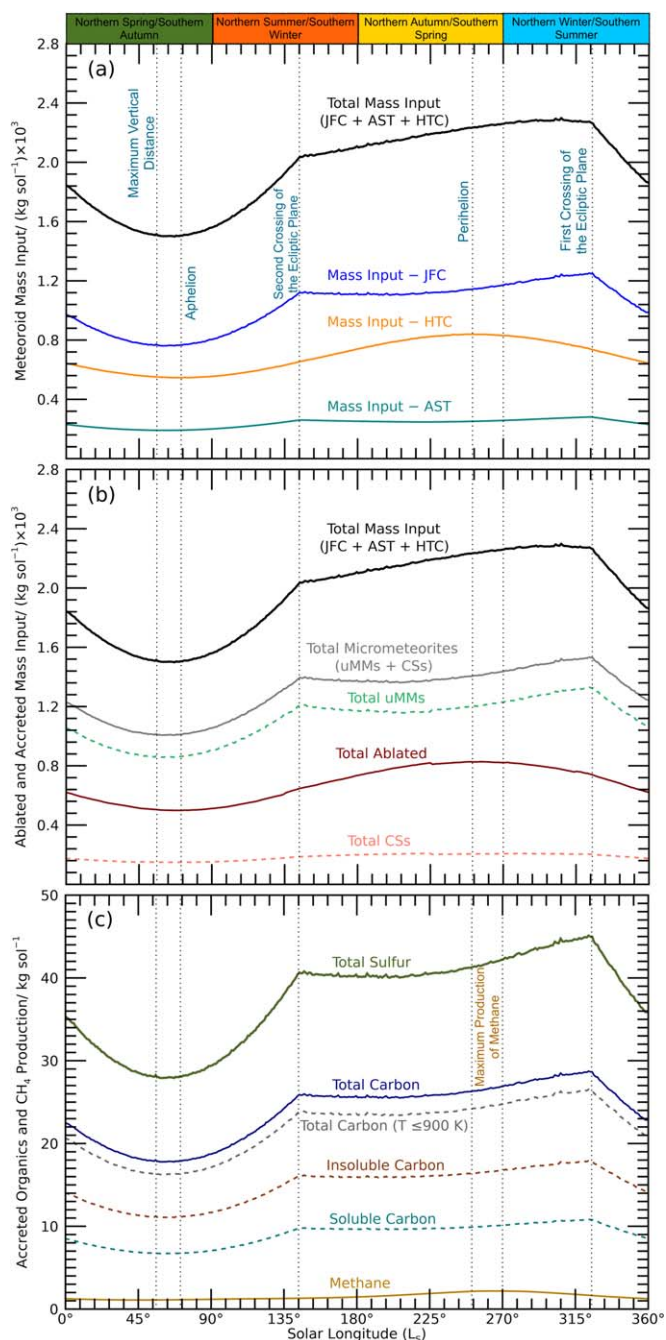


**Figure 10.** Seasonal variability of the mass fluxes, in kg sol<sup>-1</sup>, with the orbital position. Panel (a): mass fluxes of meteoroids before atmospheric entry for the JFCs (blue line), ASTs (green line), HTCs (orange line), and total mass input (black line). Panel (b): mass fluxes of total MMs (gray line), uMMs (dashed light green line), CSs (dashed red line), and total ablated (solid dark red line). Panel (c): mass fluxes of accreted sulfur (solid dark green line), total carbon (solid dark blue line), soluble and insoluble phases of carbon (dashed green and brown lines), carbon accreted from particles that do not reach the pyrolysis temperature (~900 K) during their atmospheric entry (dashed gray line), and methane production rates (solid dark yellow line) assuming a UV photolysis yield of 20%. The fluxes of carbon and methane are estimated assuming a chondritic carbon content of 5 wt% for all meteoroid populations.

average content of 2.5 wt% for all meteoroid populations. Compared with other meteoric species (see Table 1 in Carrillo-Sánchez et al. 2022), carbon and sulfur are relatively volatile species with typical ablation efficiencies 30% higher than Na and K. Interestingly, the ablation of organic matter and sulfur in the upper atmosphere of Mars may represent more than 70% of

the total ablated mass in meteoroid populations characterized by relatively slow particles, such as the JFCs and the ASTs. Consequently, even though the HTC is the main supplier of ablated organic matter and sulfur, the CABMOD-MIF model predicts that the JFCs contribute around 39% to the total ablation rates of these compounds.

Figure 10(a) displays the seasonal variability with the orbital position of the total mass influx before atmospheric ablation in  $\text{kg sol}^{-1}$  and partitioned into JFCs (blue line), ASTs (green line), and HTCs (orange line). As Carrillo-Sánchez et al. (2022) reported, the large contribution of the JFCs to the total mass input (black line) over a Martian year is consistent with observations of the zodiacal cloud (Zook 2001; Nesvorný et al. 2011; Rowan-Robinson & May 2013; Yang & Ishiguro 2015), with minimum and maximum mass inputs of  $1.50 \times 10^3$  and  $2.26 \times 10^3 \text{ kg sol}^{-1}$  at aphelion and the FCEP, respectively. Essentially, given that the JFCs and ASTs are mainly located around the ecliptic plane, their input mass rates manifest a larger increase from aphelion to the SCEP, and conversely, there is a dramatic decrease of the mass input when Mars moves away from the FCEP to aphelion.

Figure 10(b) presents the total mass influxes (black line) partitioned into total mass of accreted MMs (gray line), uMMs (dashed light green line), CSs (dashed red line), and total ablated (solid dark red line). As described above, the JFCs are the major supplier of the total accreted mass of MMs over a Martian year with minimum and maximum total fluxes of  $1.01 \times 10^3$  and  $1.52 \times 10^3 \text{ kg sol}^{-1}$  at aphelion and the FCEP, respectively, i.e., a relative increase of 50%. As indicated in the description of Table 1, most of the accreted MMs correspond to uMMs with mass influxes 6 times larger than those for the CSs. The HTCs (orange line in Figure 10(a)) are the dominant contributor to the total ablated mass (solid dark red line in Figure 10(b)) with a relative mass increase from aphelion (minimum) to perihelion (maximum) of 54% (Carrillo-Sánchez et al. 2022).

Finally, Figure 10(c) shows the mass fluxes of accreted sulfur (solid dark green line), total carbon (solid dark blue line), soluble and insoluble fractions of carbon (dashed green and brown lines), and carbon accreted from particles that do not reach the pyrolysis temperature ( $\sim 900 \text{ K}$ ) during their atmospheric entry (dashed gray line). The model predicts that more than 90% of the total accreted carbon corresponds to all those particles that did not reach the pyrolysis temperature of  $\sim 900 \text{ K}$ , and the volatile SOM fraction represents around 38% of the total accreted intact carbon at the Martian surface. Note that Figure 1 also schematically illustrates the variations of the total mass fluxes of both MMs and accreted organic carbon with  $L_S$ . The minimum and maximum accretion rates of organic carbon and sulfur are between 18 and  $28 \text{ kg sol}^{-1}$  at aphelion and  $29\text{--}45 \text{ kg sol}^{-1}$  at the FCEP, i.e., a relative increase of 60%. Likewise, assuming an average carbon content in cometary particles of 25.6 wt%, the rates of unaltered carbon increase to  $90 \text{ kg sol}^{-1}$  at aphelion and  $145 \text{ kg sol}^{-1}$  at the FCEP, while the accretion rates of sulfur decrease to  $10 \text{ kg sol}^{-1}$  at aphelion and  $15 \text{ kg sol}^{-1}$  at the FCEP for an average content of 2.5 wt% for all meteoroid sources.

In summary, the CABMOD-MIF model predicts that the JFCs are the dominant supplier of organic matter ranging from 87% for a 5 wt% in C to 96% for a 25.6 wt% in C in comets. In addition, Figures 1 and 10(c) show that the accretion rates of carbon and sulfur increase when both the heliocentric distance

and vertical distance to the ecliptic plane decrease. This is because the maximum mass contribution of accreted MMs from the JFCs and the ASTs occurs at the FCEP, since these meteoroid populations are mainly concentrated around the ecliptic plane (Nesvorný et al. 2010, 2011; Carrillo-Sánchez et al. 2022), where the vertical distance is 0 au (see Figures 1 and 10). In contrast, as shown in Figure 1, the minimum accretion of MMs is located between the maximum vertical distance to the ecliptic plane ( $L_S = 56^\circ$ ) and aphelion, with 0.054 au and 0.051 au, respectively.

Flynn (1996) inferred a flux of unaltered carbon at Mars assuming a total C content of 10 wt% of  $678 \text{ kg sol}^{-1}$  ( $339 \text{ kg sol}^{-1}$  for 5 wt% in C), that is, significantly larger than the most recent estimate of  $177 \text{ kg sol}^{-1}$  ( $88 \text{ kg sol}^{-1}$  for 5 wt% in C; Frantseva et al. 2018). In fact, Frantseva et al. (2018) contemplated for the first time a separate contribution of comets and asteroids to the total delivery of organics at the Martian surface and proposed that the ASTs were the main supplier of carbon with 79%. The discrepancy with the CABMOD-MIF model estimates is caused by two factors. First, Frantseva et al. (2018) inferred the impactor flux of cometary and asteroidal particles by modeling the orbital motion of their parent bodies but without considering the dynamical evolution of the ejected particles, whereas the DMZC model used by the MIF considers that long-time evolved particles may be completely destroyed by collisions before crossing a planet's orbit (Nesvorný et al. 2010). Second, the DMZC model is constrained by the measured orbital distribution of meteoroids, which limits the contribution of the ASTs to the total cosmic dust density of the zodiacal cloud (Nesvorný et al. 2006, 2010).

As mentioned in Section 2.3, the accretion rates of intact carbon,  $R_C$ , estimated by the CABMOD-MIF model are used to quantify the size of the organic matter reservoir at the surface,  $M_C$  (see Equation (7)), expressed as a surface density in  $\text{kg m}^{-2}$ . The mixing ratio of the total surface load of organic carbon within the near-surface regolith in parts per million (ppm) is defined as

$$\text{ppm}|_C = 10^6 \frac{M_C}{M_R} = 10^6 \frac{M_C}{d_{UV} \rho_R}, \quad (10)$$

where  $M_R$  is the areal density of the near-surface regolith in which the surface load of organics is mixed in  $\text{kg m}^{-2}$ , and  $d_{UV}$  and  $\rho_R$  are the penetration depth for UV radiation into regolith and the density of Martian regolith, respectively, assuming that the surface reservoir of carbon is well mixed with the regolith until saturation at all levels of the mixing depth. Experiments with Mars analog soils suggest a typical value of  $d_{UV}$  of  $200 \mu\text{m}$  before the 90% attenuation level is reached (Schuerger et al. 2003). With respect to the density of the Martian regolith,  $\rho_R$ , measurements at the Opportunity landing site reported a value of  $\sim 1300 \text{ kg m}^{-3}$  (Zeng et al. 2015; Llamas et al. 2022), so in this work, the surface load of carbon is considered to be mixed with up to  $0.26 \text{ kg m}^{-2}$  of regolith. Nonetheless, it should be noted that the presence of two permanent polar ice caps at Mars formed primarily of water ice and slabs of  $\text{CO}_2$  ice (Giuranna et al. 2008; Grima 2009; Ojha 2019; Arnold et al. 2022) may reduce the size of the surface reservoir of available carbon at latitudes above  $80^\circ\text{N}$  and  $80^\circ\text{S}$ , respectively, and preserve the accreted MMs from being degraded due to physical and (photo)chemical weathering at the Martian

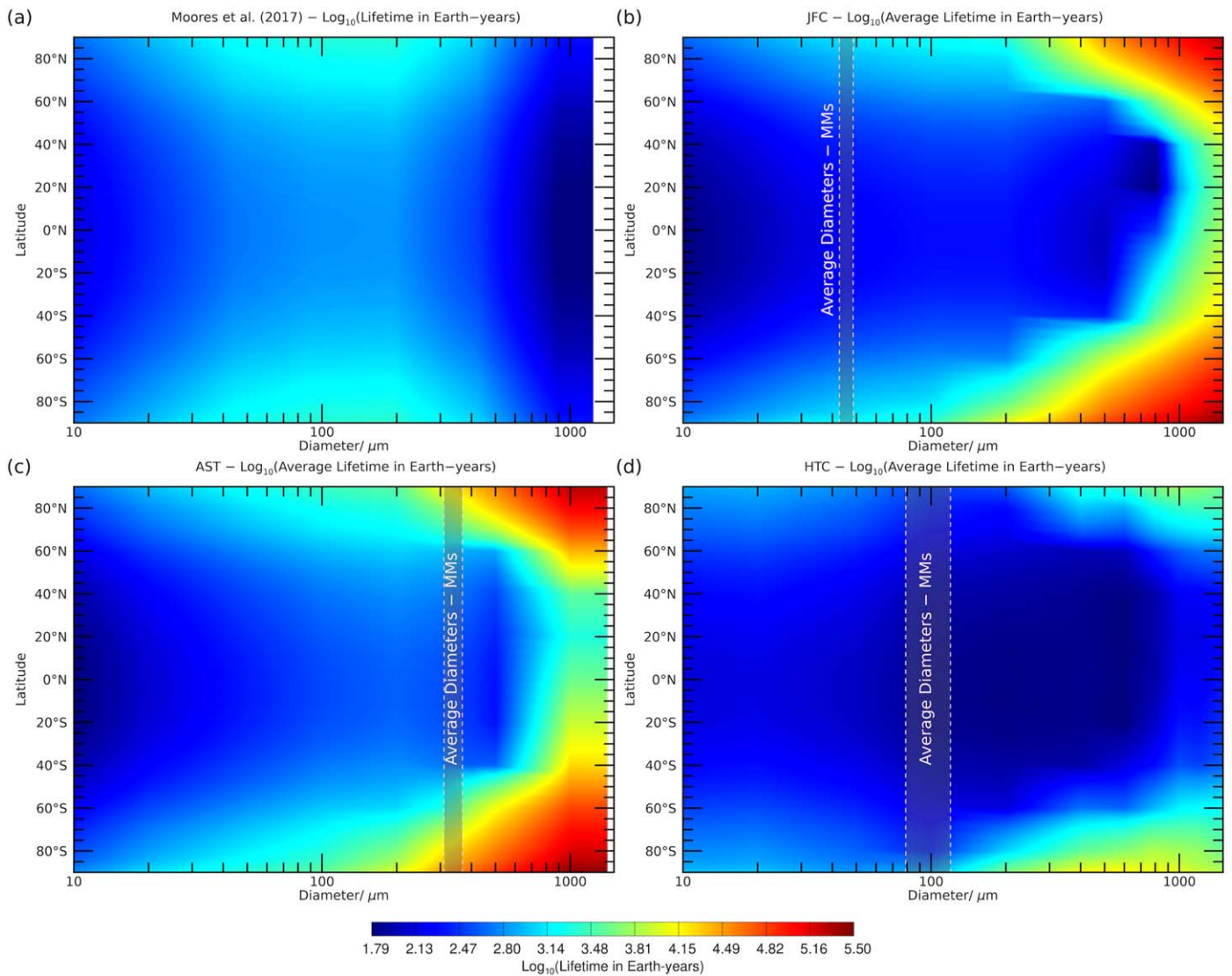


**Figure 11.** Average lifetimes of organics within the accreted particles in  $\text{Log}_{10}$ (Earth years) as a function of the Martian latitude and the particle diameter in microns. Note that the particle diameters considered in this study range from 10 to 1500  $\mu\text{m}$ . The average lifetimes predicted by the CABMOD-MIF model for the three meteoroid populations—the JFCs (b), the ASTs (c), and the HTCs (d)—are compared with the estimates provided by Moores et al. (2017) (panel (a)). Values of lifetimes range from 61.7 Earth yr (32.8 Martian yr) to  $3.16 \times 10^5$  Earth yr ( $1.68 \times 10^5$  Martian yr). The vertical dashed lines represent the range of the average typical diameters of accreted particles for each meteoroid population estimated by the CABMOD-MIF model (see also Figure 5). According to Moores et al. (2017), the fraction of MMs that survive pyrolysis during atmospheric entry decreases drastically for diameters larger than 580  $\mu\text{m}$ , tending to zero for diameters  $>1240$   $\mu\text{m}$ . In contrast, the CABMOD-MIF model estimates that there is a fraction of large MMs that do not pyrolyze in the upper atmosphere. Likewise, the differences between the calculated lifetimes in the three meteoroid sources ultimately depend on the fraction of MMs in each population that do not pyrolyze during their atmospheric entry.

surface, similar to the Earth’s poles (Taylor et al. 1998; Rojas et al. 2021). However, it is likely that the existence of flow patterns of the ice present in the Martian glaciers along with  $\text{CO}_2$  sublimation during the summertime (Baker et al. 2010; Hubbard et al. 2011) minimizes the preservation of MMs in the polar caps compared to the Earth. For simplicity, in this work, we will assume that the surface reservoir of carbon is well mixed globally with a uniform size regardless of the latitude; therefore, the presence of the permanent polar ice caps does not affect the UV degradation of organic matter within MMs.

Figure 11 presents the average lifetimes of organics within the accreted particles as a function of latitude and the particle diameter (see Equation (6) in Section 2.3), in microns, as predicted by Moores et al. (2017; Figure 11(a)) and the CABMOD-MIF model for the three meteoroid populations

(Figures 11(b)–(d)). Moores et al. (2017) considered the accretion rates of organics modeled by Flynn (1996), which are assumed to be constant with latitude and orbital position. In contrast, as discussed in Section 2.3, the CABMOD-MIF model takes account of the dynamical nature of the sporadic background of meteoroids, the separate contribution of each meteoroid population, and seasonal/latitudinal variations in the Martian atmosphere when estimating the accreted carbon at the surface. Moores et al. (2017) concluded that particles with diameters smaller than 30  $\mu\text{m}$  and larger than 400  $\mu\text{m}$  exhibit the shortest lifetimes, while there is a peak in the maximum lifetime (3500 Earth yr) for particle sizes around 150  $\mu\text{m}$  in the polar regions (Figure 11(a)). In comparison, the CABMOD-MIF model simulations indicate significantly longer lifetimes for larger particles (Figures 11(b)–(d)), so that larger particles preserve more intact carbon in the polar regions. According to

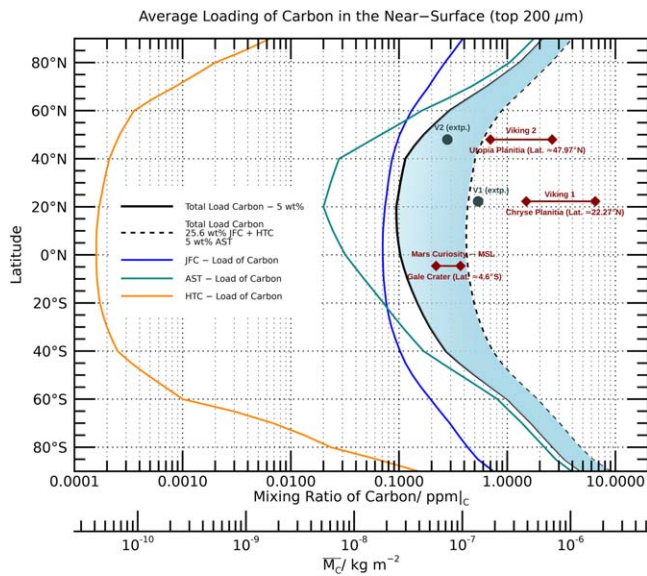


**Figure 12.** Annual average of the total surface load of carbon assuming mixing with the near-surface regolith until saturation (black lines). The solid black line represents the saturation limit assuming an average carbon content of 5 wt% for all meteoroid populations—typical for CI chondrites—and, consequently, mixing occurs below this limit. The horizontal red lines indicate the individual measurements of surface carbon for MSL (Freissinet et al. 2015) and for the Viking 1 and 2 landers (Navarro-González et al. 2010). Note that the results of MSL can be explained assuming an enrichment in carbon for cometary particles by a factor of 5.5 (blue shaded region). The gray circles represent the linear extrapolation of these mixing ratios estimated by the Viking landers for an average perchlorate content of 0.5 wt%. The contribution of each meteoroid population to the total surface load of carbon is also displayed: the JFCs (solid blue line), the ASTs (solid green line), and the HTCs (solid orange line). The dashed black line in this figure represents the total surface load assuming a carbon content for cometary particles of 25.6 wt% (see Section 2.2), and the blue shaded region shows the greatest possible range for the saturation limit of carbon in the top 200  $\mu\text{m}$  estimated by the CABMOD-MIF model. For comparison, the JFCs are the main supplier to the total surface load of organic carbon for latitudes between 50°N and 20°S and with a peak contribution at 20°N ranging from 79% to 95% for a cometary carbon content between 5 wt% and 25.6 wt%, respectively. In addition, the ASTs are the main contributor to the total surface load at high latitudes, which implies a relative contribution ranging from 83% to 47% around the poles assuming a cometary carbon content between 5 wt% and 25.6 wt%, respectively. As discussed in Section 2.2, the ASTs tend to be larger particles before entry and with velocities closer to the escape velocity of Mars; hence, a significant fraction of these bodies should penetrate deeper into the atmosphere without ablating, leading to an accretion of larger MMs with a higher content of intact carbon at northern/southern high latitudes (see Figures 5(b) and 6(b)). Consequently, even though the ASTs are a minor mass contributor to the overall flux of accreted carbon compared to the JFCs, this meteoroid source should contribute larger MMs to the surface reservoir with comparatively longer lifetimes at northern/southern high latitudes (see Figure 11(c)).

Table 1 in Flynn (1996), the fraction of MMs that survive pyrolysis during atmospheric entry decreases drastically for diameters larger than 580  $\mu\text{m}$ , being null for diameters  $>1240 \mu\text{m}$ . In contrast, the CABMOD-MIF model estimates that there is a fraction of large MMs that do not pyrolyze in the upper atmosphere. On the one hand, the MIF model for Mars predicts that there is a significant fraction of meteoroids in both the JFCs and the ASTs with velocities close to the escape velocity of Mars,  $v_{\text{esc}} = 5.03 \text{ km s}^{-1}$  (see Figure 3); on the other hand, the CABMOD model estimates that particles with diameters of 1500  $\mu\text{m}$  and velocities close to  $v_{\text{esc}}$  exhibit negligible ablation efficiencies (see Figure 8 in Carrillo-Sánchez et al. 2022), and, consequently, these particles are able to preserve a greater amount of intact carbon. Nevertheless, as discussed in Section 2.2, these larger MMs are not representative of the size distributions for the three meteoroid populations. Note that the vertical dashed lines in Figures 11(b)–(d) represent the typical average diameters of the accreted particles derived by the CABMOD-MIF model for the JFCs, the ASTs, and the HTCs (see also Figure 5).

Figures 11(b)–(d) also show that, for comparison, the ASTs exhibit the longest-lived MMs, with 1640 Earth yr at the equatorial band and 36,700 and 67,200 Earth yr at the north and south poles, respectively, for a typical average diameter of  $\sim 350 \mu\text{m}$ . Conversely, the HTCs are the shortest-lived particles, with 76 Earth yr at the equator and 340 and 865 Earth yr at the north and south poles, respectively, for an average diameter of  $\sim 100 \mu\text{m}$ . Finally, organics in the JFCs have lifetimes of 720 Earth yr at the equator and 3800 and 4600

Earth yr at the north and south poles, respectively, for a typical average diameter of  $\sim 45 \mu\text{m}$ . The differences between the calculated lifetimes in the three meteoroid sources ultimately depend on the fraction of MMs in each population that do not pyrolyze during atmospheric entry for a given particle diameter, i.e.,  $\bar{f}_{P,n}(\phi)$  in Equation (6). Since the HTCs are mainly populated by relatively faster bodies that experience considerable heating during their atmospheric entry (see Figure 3), their values of  $\bar{f}_{P,n}(\phi)$  became significantly lower than those for the JFCs and the ASTs. Consequently, the CABMOD-MIF model indicates that the JFCs and the ASTs preserve a higher content of accreted carbon at the Martian surface than the HTCs for a given diameter; and the higher the carbon content within an accreted MM, the longer the required time to fully degrade it by UV radiation.

The solid black line in Figure 12 describes both the total mixed carbon load in the near surface assuming 200  $\mu\text{m}$  penetration of UV radiation into regolith (in ppm; see Equation (10)) and the annual average of the total surface load of unaltered carbon ( $\bar{M}_C$ , in  $\text{kg m}^{-2}$ ); basically, it represents the saturation limit of carbon in the near surface assuming a CI-chondritic carbon content for all meteoroid populations of 5 wt%. Figure 12 also shows the relative contribution of each meteoroid population to the total surface load of carbon: the JFCs (solid blue line), the ASTs (solid green line), and the HTCs (solid orange line). The dashed black line in this figure represents the total surface load assuming a carbon content for cometary particles of 25.6 wt% (see Section 2.2), and the blue shaded region shows the greatest possible range for the saturation limit of carbon in the top 200  $\mu\text{m}$  estimated by the CABMOD-MIF model. For comparison, the JFCs are the main supplier to the total surface load of organic carbon for latitudes between 50°N and 20°S and with a peak contribution at 20°N ranging from 79% to 95% for a cometary carbon content between 5 wt% and 25.6 wt%, respectively. In addition, the ASTs are the main contributor to the total surface load at high latitudes, which implies a relative contribution ranging from 83% to 47% around the poles assuming a cometary carbon content between 5 wt% and 25.6 wt%, respectively. As discussed in Section 2.2, the ASTs tend to be larger particles before entry and with velocities closer to the escape velocity of Mars; hence, a significant fraction of these bodies should penetrate deeper into the atmosphere without ablating, leading to an accretion of larger MMs with a higher content of intact carbon at northern/southern high latitudes (see Figures 5(b) and 6(b)). Consequently, even though the ASTs are a minor mass contributor to the overall flux of accreted carbon compared to the JFCs, this meteoroid source should contribute larger MMs to the surface reservoir with comparatively longer lifetimes at northern/southern high latitudes (see Figure 11(c)).

In summary, the CABMOD-MIF model yields a mixing ratio of organic carbon ranging from 0.09–0.43 ppm for a latitude of 20°N to 4.8–8.9 ppm at 90°S. Moores et al. (2017) reported values of the mixing ratios between  $\sim 2.8$ –14.3 ppm at 20°N and  $\sim 13.9$ –71.2 ppm at 80° S. Note that the estimates of Moores et al. (2017) have been scaled to carbon contents of 5 wt% and 25.6 wt%, respectively, for an appropriate comparison. The main reason for this disagreement is that, as discussed above, the accretion rates of carbon estimated by Flynn (1996) are on average a factor of  $\sim 15$  higher than those derived by the CABMOD-MIF model. The horizontal red lines in Figure 12 indicate the ranges for the mixing ratios of carbon inferred for

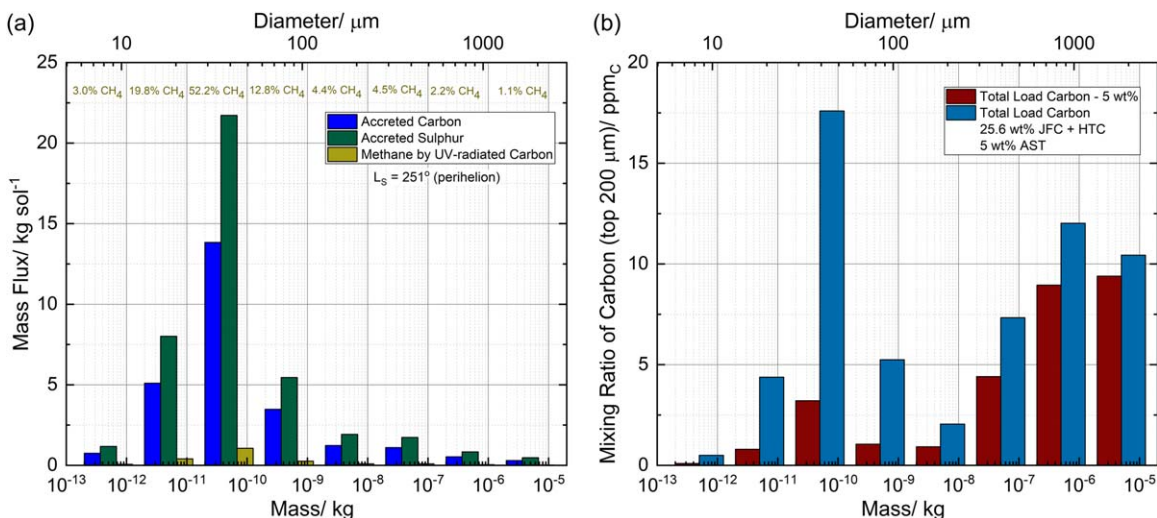


**Figure 13.** Panel (a): mass histograms of the accretion rate of carbon (dark blue) and sulfur (dark green), along with the methane production rates generated by surface carbon assuming a UV photolysis yield of 20% (light green) at  $L_s = 251^\circ$  (perihelion) for average carbon and sulfur contents of 5 wt% and 7 wt%, respectively. Panel (b): mass histograms of the mixing ratios of carbon in the top 200  $\mu\text{m}$  assuming an average carbon content of 5 wt% (dark red) and 25.6 wt% (light blue) for cometary particles.

the MSL (Gale crater, latitude =  $4.6^\circ\text{S}$ ; Freissinet et al. 2015), and for the Viking 1 lander (Chryse Planitia, latitude =  $22.3^\circ\text{N}$ ) and the Viking 2 lander (Utopia Planitia,  $48^\circ\text{N}$ ; Navarro-González et al. 2010). First, the MSL inferred a mixing ratio of organics between 0.2 and 0.4 ppm that may be explained by the CABMOD-MIF simulations assuming an enrichment in the carbon content of cometary particles. Second, in order to explain the results from the Viking lander missions, Navarro-González et al. (2010) developed a kinetic model and derived a mixing ratio of organics for the Viking 1 lander ranging from 1.5 ppm in the presence of 0.1% perchlorate to 6.5 ppm in the presence of 0.01% perchlorate, whereas for the Viking 2 lander, the values are between 0.7 ppm and 2.6 ppm for perchlorate levels between 0.1% and 0.01%, respectively.

In principle, as shown in Figure 12, the CABMOD-MIF model cannot reproduce these estimates for the Viking landers, even assuming an enrichment in the carbon content of cometary particles. Nonetheless, the SAM instrument on board the MSL rover detected perchlorate salts at levels of 0.4–0.6 wt% (Glavin et al. 2013) that are homogeneously distributed across the Martian surface (Archer et al. 2014), being the best candidate hydrated calcium perchlorate ( $\text{Ca}(\text{ClO}_4)_2 \cdot n\text{H}_2\text{O}$ ). As a result, a higher content in perchlorates in the Martian regolith would lead to a marked decrease in the mixing ratios of organic carbon inferred by Navarro-González et al. (2010). The gray circles in Figure 12 represent the linear extrapolation of these mixing ratios assuming an average perchlorate content of 0.5 wt%, which is in better agreement with the CABMOD-MIF simulations. Nonetheless, the extrapolated estimate for the Viking 1 lander is still above the modeled upper saturation limit of carbon, and this disagreement may be due to several factors: (1) the CABMOD-MIF model does not consider any redistribution of the accreted MMs across the Martian regolith (see discussion in Section 2.2); (2) the carbon content in cometary particles may be higher than the average estimate of 25.6 wt%, such as for comet 67P/Churyumov–Gerasimenko, which is depleted in Mg but exhibits a carbon content of 42 wt% (see Table 3 in Bardyn et al. 2017); and (3) there are indigenous mechanisms at the Martian surface that might give rise to the further formation of organics, such as formation

through water–rock interactions (Sharma et al. 2023), along with the electrochemical reduction of aqueous  $\text{CO}_2$  to organic molecules through interactions with soil minerals (Steele et al. 2018). Moreover, apart from the uncertainties inherent in the measurements of the Curiosity/MSL rover and the Viking landers, it is important to note that the presence of organics at the Martian regolith would be challenging to measure given that the detection probability of current techniques such as pyrolysis Fourier transform infrared spectroscopy is  $\sim 17\%$  in the 4–21 ppm range and  $\sim 56\%$  in the 22–43 ppm range (Gordon & Sephton 2016).

Figure 13(a) shows mass histograms of the accretion of unaltered carbon (dark blue bars) and sulfur (dark green bars) predicted by the CABMOD-MIF model for an average chondritic content of carbon and sulfur of 5 wt% and 7 wt%, respectively, at perihelion; note that the mass distribution of the accreted compounds predicted by the CABMOD-MIF model does not change significantly with  $L_s$ . The CABMOD-MIF model estimates that  $\sim 75\%$  of the unaltered carbon-bearing particles at the Mars surface are smaller than 40  $\mu\text{m}$  diameter. Figure 13(b) shows mass histograms of the mixing ratios of carbon in the top 200  $\mu\text{m}$  assuming an average carbon content of 5 wt% (dark red) and 25.6 wt% for cometary particles (light blue) and represents the mass distributions for the case of a complete redistribution of the accreted MMs over the Mars surface. For comparison, the carbon reservoir is shifted to particles larger than 300  $\mu\text{m}$  diameter for a carbon content of 5 wt%, where the ASTs are the main contributor of the reservoir, whereas an enrichment in carbon for cometary particles gives rise to a peak around 40  $\mu\text{m}$  diameter that corresponds to the JFCs.

### 3.3. Constraints on the Potential Methane Production at the Mars Surface

In this section, we address the generation of methane by UV photolysis of the carbon reservoir at the Martian surface predicted by the CABMOD-MIF model, along with an assessment of the factors that would contribute to a background level below the most recent detections by the Atmospheric Chemistry Suite (ACS) on board ExoMars/TGO (Montmessin et al. 2021). It should be noted

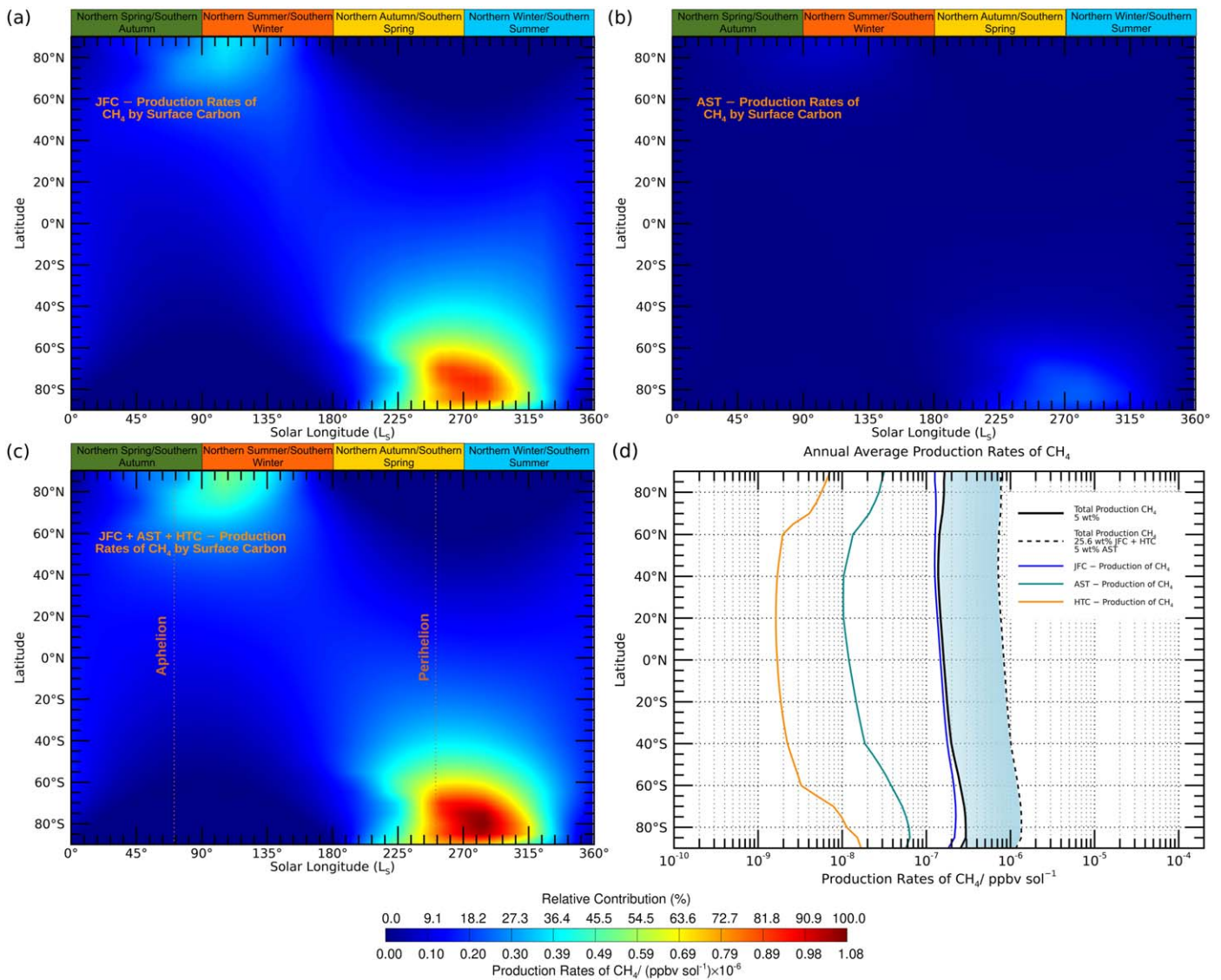


**Figure 14.** Panels (a), (b), and (c): seasonal variability of the equivalent column concentration of the methane rates generated by UV-radiated surface carbon, in ppbv sol<sup>-1</sup>, assuming a UV photolysis yield of 20% and for the JFCs (a); the ASTs (b); and the total, JFCs + ASTs + HTCs (c), in terms of the Martian latitude and solar longitude. Note that seasonal variations of the methane rates of the HTCs are not displayed in this figure given its negligible contribution to the total flux. The methane rates are calculated assuming a chondritic carbon content of 5 wt%. Panel (d): annual average of the equivalent column concentration of methane assuming an average carbon content of 5 wt% for all meteoroid populations (solid black line). The blue shaded region in panel (d) represents the average methane production rate between a chondritic composition and a carbon content of 25.6 wt% for particles with a cometary origin (dashed black line). The contribution of each meteoroid population to the total accretion rates of carbon is also displayed in panel (d): the JFCs (solid blue line), the ASTs (solid green line), and the HTCs (solid orange line).

that the methane generated by UV photolysis is subject to both subsequent global transport dynamics and chemical removal; therefore, the abundance of methane produced by UV photolysis of accreted carbon should be implemented within a global circulation model of Mars for a more accurate estimate of the geographical and seasonal redistributions, particularly if the atmospheric lifetime is much shorter than the estimates of over 300 yr (Grenfell et al. 2022). However, the assessment of the dynamical evolution of the methane abundances in the Martian atmosphere is out of the scope of this work. Figure 14 presents the seasonal variability of the equivalent column concentration of the methane rates generated by UV-radiated surface carbon, in ppbv sol<sup>-1</sup>, for the JFCs (panel (a)), the ASTs (panel (b)), and the total, JFCs + ASTs + HTCs (panel (c)), in terms of latitude and  $L_s$  and assuming a reaction yield of the conversion of the surface organic carbon into methane of 20% (Schuerger et al. 2012). The seasonal

variation of the methane rates produced from HTCs is not displayed in Figure 14 given its negligible contribution to the total flux. For comparison, the JFCs are the main contributor to the methane rates given that this source is characterized by smaller particle sizes that have significantly shorter methane photoproduction lifetimes than the larger ASTs (see Figure 11). In fact, Figure 13 shows that around 88% of the methane is produced by particles smaller than 100  $\mu\text{m}$  diameter and peaking at  $\sim 40 \mu\text{m}$  (light green bars). Similar to the result of Moores et al. (2017) and Moores & Schuerger (2012), Figure 14(c) shows that the largest peaks in methane production occur around polar latitudes during the summer, reflecting the location of the carbon reservoir (see Figure 12) and the seasonal variability of UV radiation (Figure 7(b)). As a result, the summertime methane production rates are  $5.09 \times 10^{-7}$  ppbv sol<sup>-1</sup> at 80°N and  $1.08 \times 10^{-6}$  ppbv sol<sup>-1</sup> at 80° S, between 3 and 7 times larger than the average flux

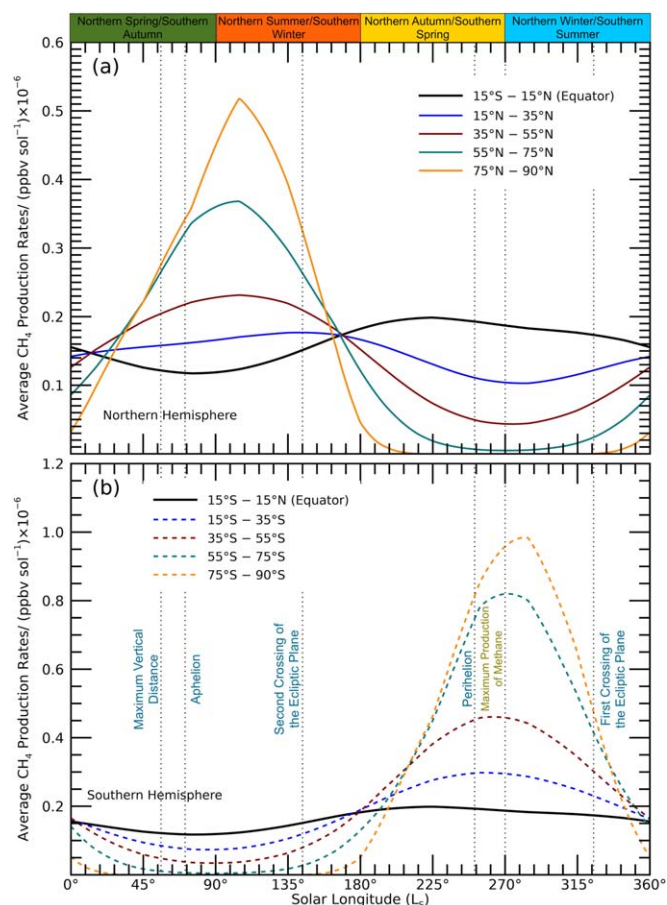


**Figure 15.** Seasonal variability of the equivalent column concentration of methane, in  $\text{ppbv sol}^{-1}$ , generated by UV-radiated surface carbon assuming a UV photolysis yield of 20% and averaged over different latitudinal bands for the northern hemisphere (panel (a)) and the southern hemisphere (panel (b)). Note that the methane rates are calculated assuming a chondritic carbon content of 5 wt% for all meteoroid populations.

of  $1.57 \times 10^{-7} \text{ ppbv sol}^{-1}$  in the equatorial region. Additionally, the peak of methane flux during the summer is 2 times higher in the south pole than in the north pole due to the comparatively lower surface load of carbon in the northern hemisphere (see Figures 6 and 12). Figure 14(d) represents the annual average of the equivalent column concentration of methane assuming an average carbon content of 5 wt% for all meteoroid populations (solid black line). The blue shaded region represents the average methane production rates between a chondritic composition and a carbon content of 25.6 wt% for particles with a cometary origin (dashed black line). The contribution of each meteoroid population to the total accretion rates of carbon is also displayed in Figure 14(d).

The solid yellow line in Figure 10(c) describes the seasonal variability of the methane production rates compared with the accretion rates of carbon for a chondritic carbon content of 5 wt% for all meteoroid populations. The minimum and maximum fluxes of methane occur around aphelion and perihelion with 1 and 2  $\text{kg sol}^{-1}$  (see Table 1 and Figure 1), respectively, with a relative contribution of 87% for the JFCs, 12% for the ASTs, and 1% for the HTC. If the carbon content in cometary particles is assumed to be 25.6 wt%, the production rates of methane range from 6 to 11  $\text{kg sol}^{-1}$  at aphelion and perihelion, respectively, increasing the relative contribution of the JFCs up to 96% (see values in italics in Table 1).

Figure 15 describes the seasonal variability of the equivalent column concentration of methane generated by UV-radiated surface carbon averaged over different latitudinal bands, in  $\text{ppbv sol}^{-1}$ , for the northern hemisphere (panel (a)) and the southern hemisphere (panel (b)) for a carbon content of 5 wt%. Figure 15 shows that the methane production rates in the northern hemisphere above  $55^\circ\text{N}$  (solid green and yellow lines in Figure 15(a)) and in the southern hemisphere for latitudes below  $35^\circ\text{S}$  (red, green, and yellow dashed lines in Figure 15(b)) are mainly constrained by the seasonal changes of the UV radiation due to the convolution of the axial tilt and the eccentricity of Mars' orbit (see Figure 7), with maximum and minimum methane rates around the summer and winter, respectively. In contrast, the black solid lines in Figures 15(a) and (b) show that the methane fluxes in the equatorial band ( $15^\circ\text{S}$ – $15^\circ\text{N}$ ) are less perturbed by the seasonal variability of the UV radiation. It should be noted that the background levels of methane measured by the Mars Curiosity at the Gale crater over a 5 yr period (Webster et al. 2018) cannot only be explained by the modeled seasonal variations of the methane rates presented in this study, and it may be potentially caused by diffusion through the regolith of methane supplied from below by microseepage rather than UV degradation of exogenous carbon (Moores et al. 2019a, 2019b, 2024).

Lefèvre & Forget (2009) estimated that the global average  $e$ -folding lifetime of methane is 330 Earth yr, which is consistent with previous estimates that ranged between 250 and 670 yr (Summers et al. 2002; Wong et al. 2003; Krasnopolsky et al. 2004; Atreya et al. 2007). Using a lifetime of 329 yr (Moores & Schuerger 2012), the CABMOD-MIF model organic accretion rate would produce a steady-state methane mixing ratio of 0.021 ppbv assuming a chondritic carbon content of 5 wt% for all meteoroid populations and a reaction yield for the methane production of 20%, or 0.11 ppbv for an average carbon content in cometary particles of 25.6 wt%. This spread of methane mixing ratios is below the 0.5–11 ppbv range shown in Figure 5(c) in Moores et al. (2017).

In terms of recent measurements of global background methane, Korablev et al. (2019) and Knutsen et al. (2021) used the NOMAD spectrometer on ExoMars/TGO to determine an upper limit of 0.06 ppbv for all latitudes between  $85^\circ\text{N}$  and  $85^\circ\text{S}$  and over the altitude range from 6 to 100 km. Most recently, measurements performed in the vicinity of the Gale crater by the ACS instrument on board ExoMars/TGO reported an annual mean upper limit of only 0.02 ppbv (Montmessin et al. 2021). The CABMOD-MIF simulations therefore estimate a mixing ratio of methane that is a factor of up to 5 times larger than this upper limit, and there are two probable reasons that may decrease these results. First, the photochemical production yield of methane from surface organic carbon may be overestimated, being lower than 20%. Second, there may be unknown physical and/or chemical processes that shorten the methane lifetime.

Concerning the photochemical yield of methane, the H/C ratio of the organics within an accreted particle is probably important, since it is unlikely that methane is the only photochemical product generated by UV photolysis (Moores et al. 2017). Accordingly, the fraction of methane generated with respect to other products has been shown to depend on the ratio H/C (Schuerger et al. 2012): the higher the H/C ratio, the greater the fraction of organic matter converted to methane. In general, a H/C elemental ratio close to 1 suggests the presence of unsaturated compounds rather than aliphatic compounds (Bones et al. 2022). Recently, the

**Table 2**

Background Mixing Ratios of CH<sub>4</sub> on Mars as Estimated by the CABMOD-MIF Model: Lifetimes of CH<sub>4</sub> in Earth Years (First Column), Reaction Yield to Produce CH<sub>4</sub> by Surface Carbon in % (Second Column), Carbon Content in Meteoroids in wt% (Third Column), and Average Background of CH<sub>4</sub> in ppbv (Fourth Column)

Lifetime of CH <sub>4</sub> in Earth years	Reaction Yield ( $\bar{Y}_{\text{CH}_4}$ ) to Produce CH <sub>4</sub> by UV Photolysis in %	Carbon Content in Meteoroids in wt%	Average Background of CH <sub>4</sub> in ppbv
329 <sup>a</sup>	20	5 <sup>b</sup>	0.021
329	10	5	0.011
329	20	25.6 <sup>d</sup>	0.11
59.8	20	25.6	0.02 <sup>c</sup>
329	3	25.6	0.02

**Notes.** The value in italics represents the corresponding methane lifetime recalculated to explain the upper limit of 0.02 ppbv measured by ExoMars/TGO (Montmessin et al. 2021).

<sup>a</sup> Lefèvre & Forget (2009).

<sup>b</sup> Total C content in CI chondrites (Lodders & Fegley 2011).

<sup>c</sup> Upper limit of CH<sub>4</sub> measured by the ACS on board ExoMars/TGO (Montmessin et al. 2021).

<sup>d</sup> The carbon content only increases for particles with a cometary origin.

Rosetta orbiter to comet 67P/Churyumov–Gerasimenko analyzed 33 different cometary particles collected from the coma and found a mean H/C ratio of  $1.04 \pm 0.16$ , indicating that particles of cometary origin are less unsaturated than organic matter in MMs (Isnard et al. 2019). Likewise, Schuerger et al. (2012) assumed a 20% conversion rate for the production rate of methane, which corresponds to an average H/C ratio within MMs of 0.2. A second factor is that atomic H is produced photochemically through H<sub>2</sub>O photolysis in the lower atmosphere (Krasnopolsky 2006), and this may help to increase the H/C ratio through heterogeneous reactions with unsaturated organics in the surface layer. A third factor would be the existence of soil oxidants at the Martian surface, such as perchlorate salts (Hecht et al. 2009; Glavin et al. 2013); while these may lead to disaggregation of MMs, allowing UV radiation access to the particle interior spaces (see Section 2.3), the presence of perchlorates in combination with other potential oxidants generated via irradiation by cosmic rays, such as H<sub>2</sub>O<sub>2</sub>, might also compete with the UV photolysis, decreasing the available organic carbon at the Martian regolith that might have been converted into methane.

With respect to the methane atmospheric lifetime, Grenfell et al. (2022) recently suggested two factors that might reduce the methane lifetime to only 21 yr: first, an increase in the H<sub>2</sub>O column abundance leading to a higher OH radical concentration, and second, a higher Cl atom concentration produced from exposed perchlorate salts at the surface.

Table 2 shows the background mixing ratio of methane on Mars, in ppbv, as estimated by the CABMOD-MIF model for two different carbon contents, that is, assuming 5 wt% for all meteoroid populations and 25.6 wt% only for particles with cometary origin. As discussed above, assuming a methane yield of 20% (Schuerger et al. 2012) and an atmospheric lifetime of 329 Earth yr (Lefèvre & Forget 2009; Moores & Schuerger 2012), the predicted methane mixing ratio is close to the 0.02 ppbv upper limit from ExoMars/TGO (Montmessin et al. 2021) if meteoroids from all sources have a carbon content of 5 wt%. For the more likely case of 25.6 wt% C in

cometary particles, either the atmospheric lifetime has to be reduced to 59.8 Earth yr, or the reaction yield has to be reduced to 3%. Bearing in mind the reasons discussed above that would produce a shorter lifetime and/or lower photochemical yield, we conclude that the CABMOD-MIF results are in sensible accord with the ExoMars/TGO observations.

#### 4. Summary and Conclusions

In this study, we present a comprehensive model to quantify the ablation of exogenous organic matter in the Martian upper atmosphere, along with the accretion of intact carbon at the surface. The model accounts for the latitudinal and seasonal fluctuations of the most relevant meteoroid populations in the inner solar system: JFCs, ASTs, and HTC. For this purpose, we have updated the CABMOD (Carrillo-Sánchez et al. 2020a) with a semiempirical model describing the pyrolysis kinetics during the ablation process of both the relatively volatile SOM and the relatively refractory IOM (Bones et al. 2022). CABMOD is then combined with the MIF (Jancheš et al. 2020; Carrillo-Sánchez et al. 2022) that characterizes the diurnal, latitudinal, and seasonal distribution of meteoroids entering Mars' atmosphere. In summary, the modeling results indicate the following:

1. The global injection rates of carbon and sulfur into the upper atmosphere are 52 and 82 kg sol<sup>-1</sup> at aphelion and 78 and 122 kg sol<sup>-1</sup> at perihelion, respectively, considering a CI-chondritic composition for all meteoroid populations (5 wt% C and 7 wt% S). Assuming an average carbon content in cometary particles of 25.6 wt%, the injection rates of carbon range from 256 to 387 kg sol<sup>-1</sup> at aphelion and perihelion, respectively. Similarly, the fluxes of sulfur vary between 28 and 42 kg sol<sup>-1</sup> at aphelion and perihelion, respectively, for an average content of sulfur of 2.5 wt%.
2. The minimum and maximum accretion rates of organic carbon and sulfur at the Martian surface are between 18 and 28 kg sol<sup>-1</sup> at aphelion and 29 and 45 kg sol<sup>-1</sup> at the FCEP. Assuming an average carbon content in cometary particles of 25.6 wt%, the rates of unaltered carbon increase to 90 kg sol<sup>-1</sup> at aphelion and 134 kg sol<sup>-1</sup> at the FCEP. Likewise, the deposition rates of sulfur decrease to 10 kg sol<sup>-1</sup> at aphelion and 15 kg sol<sup>-1</sup> at the FCEP for a sulfur content of 2.5 wt%.
3. A total of ~88% of the unaltered carbon-bearing particles at the Mars surface are smaller than 100 μm diameter, with a peak size around 40 μm.
4. The mixing ratios of the organic carbon in the Martian surface range from 0.09 to 0.43 ppm for a latitude of 20° N to 2.7–4.7 ppm at 80°S, in reasonably good agreement with measurements inferred by the Mars Curiosity at the Gale crater (Freissinet et al. 2015) and the Viking lander missions (Navarro-González et al. 2010).

The accretion of organic carbon at the Martian regolith creates a surface reservoir that may be potentially degraded by UV irradiation to yield methane (Moores et al. 2007; Schuerger et al. 2011, 2012). The minimum and maximum fluxes of methane occur around aphelion and perihelion with 1 and 2 kg sol<sup>-1</sup>, respectively, with a relative contribution of 87% from the JFCs, 12% from the ASTs, and 1% from the HTCs. If the carbon content in cometary particles is assumed to be 25.6 wt%, the production rates of methane range from 6 to 11 kg sol<sup>-1</sup> at aphelion and perihelion, respectively, increasing

the relative contribution of the JFCs up to 96%. Assuming a lifetime of 329 Earth yr (Moore & Schuerger 2012), the CABMOD-MIF model infers a background mixing ratio of methane on Mars ranging from 0.021 ppbv to 0.11 ppbv — for a C content in comets between 5 wt% and 25.6 wt%, respectively. To explain the upper limit of 0.02 ppbv measured by ExoMars/TGO (Montmessin et al. 2021), either the atmospheric lifetime has to be reduced to 59.8 Earth yr, or the reaction yield has to be reduced to 3% for the more likely case of 25.6 wt% C in cometary particles.

### Acknowledgments

This work is supported by NASA's Planetary Science Division Research Program through work package Exospheres, Ionospheres, Magnetospheres Modeling (EIMM). J.M.C.P. is supported by the UK Science and Technology Facilities Council (project ST/T000279/1). G.L.V. acknowledges funding from the Planetary Science Division Internal Scientist Funding Program through the Fundamental Laboratory Research (FLaRe) work package. The CABMOD-MIF output is available upon request to J.D.C.S., J.M.C.P., or D.J. The CABMOD model has been optimized using the GNU Parallel shell tool (version 20190922) (Tange 2018).

### ORCID iDs

Juan Diego Carrillo-Sánchez  <https://orcid.org/0000-0001-8230-4048>

John M. C. Plane  <https://orcid.org/0000-0003-3648-6893>

Diego Janches  <https://orcid.org/0000-0001-8615-5166>

Gerónimo L. Villanueva  <https://orcid.org/0000-0002-2662-5776>

### References

- Acton, C. H. 1996, *P&SS*, **44**, 65
- Alexander, C. M. O., Wynn, J. G., & Bowden, R. 2022, *M&PS*, **57**, 334
- Altwegg, K., Balsiger, H., Bar-Nun, A., et al. 2016, *SciA*, **2**, e1600285
- Anders, E. 1989, *Natur*, **342**, 255
- Andersson, L., Weber, T. D., Malaspina, D., et al. 2015, *Sci*, **350**, aad0398
- Archer, P. D. 2010, PhD thesis, Univ. Arizona, <http://hdl.handle.net/10150/195892>
- Archer, P. D., Franz, H. B., Sutter, B., et al. 2014, *JGRE*, **119**, 237
- Arnold, N. S., Butcher, F. E. G., Conway, S. J., Gallagher, C., & Balme, M. R. 2022, *NatAs*, **6**, 1256
- Atreya, S. K., Mahaffy, P. R., & Wong, A.-S. 2007, *P&SS*, **55**, 358
- Baker, D. M. H., Head, J. W., & Marchant, D. R. 2010, *Icar*, **207**, 186
- Bardyn, A., Baklouti, D., Cottin, H., et al. 2017, *MNRAS*, **469**, S712
- Basiuk, V. A., & Douda, J. 1999, *P&SS*, **47**, 577
- Benner, S. A., Devine, K. G., Matveeva, L. N., & Powell, D. H. 2000, *PNAS*, **97**, 2425
- Bergin, E. A., Blake, G. A., Ciesla, F., Hirschmann, M. M., & Li, J. 2015, *PNAS*, **112**, 8965
- Biemann, K., Oro, J., Toulmin, P., et al. 1976, *Sci*, **194**, 72
- Bones, D. L., Carrillo Sánchez, J. D., Connell, S. D. A., et al. 2022, *E&SS*, **9**, e01884
- Bones, D. L., Carrillo-Sánchez, J. D., Kulak, A. N., & Plane, J. M. C. 2019, *P&SS*, **179**, 104725
- Brown, P., Weryk, R. J., Wong, D. K., & Jones, J. 2008, *Icar*, **195**, 317
- Brownlee, D. E. 1985, *AREPS*, **13**, 147
- Carrier, B. L., & Kounaves, S. P. 2015, *GeoRL*, **42**, 3739
- Carrillo-Sánchez, J. D., Bones, D. L., Douglas, K. M., et al. 2020a, *P&SS*, **187**, 104926
- Carrillo-Sánchez, J. D., Gómez-Martín, J. C., Bones, D. L., et al. 2020b, *Icar*, **335**, 113395
- Carrillo-Sánchez, J. D., Janches, D., Plane, J. M. C., et al. 2022, *PSJ*, **3**, 239
- Carrillo-Sánchez, J. D., Nesvorný, D., Pokorný, P., Janches, D., & Plane, J. M. C. 2016, *GeoRL*, **43**, 11979
- Carrillo-Sánchez, J. D., Plane, J. M. C., Feng, W., Nesvorný, D., & Janches, D. 2015, *GeoRL*, **42**, 6518
- Chyba, C., & Sagan, C. 1992, *Natur*, **355**, 125
- Cordier, C., Van Ginneken, M., & Folco, L. 2011, *M&PS*, **46**, 1110
- Court, R. W., & Sephton, M. A. 2011, *GeCoA*, **75**, 1704
- Crandall, P. B., Gobi, S., Gillis-Davis, J., & Kaiser, R. I. 2017, *JGRE*, **122**, 1880
- Dawkins, E. C. M., Stober, G., Carrillo-Sánchez, J. D., et al. 2023, *P&SS*, **238**, 105796
- DeLuca, M., Sternovsky, Z., Armes, S. P., et al. 2022, *JGRE*, **127**, e2021JE007168
- Duffie, J. A., & Beckman, W. A. 2013, *Solar Engineering of Thermal Processes* (New York: Wiley)
- Eigenbrode, J. L., Summons, R. E., Steele, A., et al. 2018, *Sci*, **360**, 1096
- Flynn, G. J. 1996, *EM&P*, **72**, 469
- Flynn, G. J., Consolmagno, G. J., Brown, P., & Macke, R. J. 2018, *ChEG*, **78**, 269
- Flynn, G. J., Keller, L. P., Feser, M., Wirick, S., & Jacobsen, C. 2003, *GeCoA*, **67**, 4791
- Frantseva, K., Mueller, M., ten Kate, I. L., van der Tak, F. F. S., & Greenstreet, S. 2018, *Icar*, **309**, 125
- Fraser, W. C., Dones, L., Volk, K., Womack, M., & Nesvorný, D. 2022, arXiv:2210.16354
- Freissinet, C., Glavin, D. P., Mahaffy, P. R., et al. 2015, *JGRE*, **120**, 495
- Genge, M. J. 2017, *GeoRL*, **44**, 1679
- Genge, M. J., & Grady, M. M. 1998, *M&PS*, **33**, 425
- Giuranna, M., Grassi, D., Formisano, V., et al. 2008, *Icar*, **197**, 386
- Glavin, D. P., & Bada, J. L. 2001, *AsBio*, **1**, 259
- Glavin, D. P., Freissinet, C., Miller, K. E., et al. 2013, *JGRE*, **118**, 1955
- Gomez Martin, J. C., Bones, D. L., Carrillo-Sanchez, J. D., et al. 2017, *API*, **836**, 212
- Gordon, P. R., & Sephton, M. A. 2016, *AsBio*, **16**, 831
- Grady, M. M., & Wright, I. 2006, *RSPTB*, **361**, 1703
- Grenfell, J. L., Wunderlich, F., Sinnhuber, M., et al. 2022, *Icar*, **382**, 114940
- Greshake, A., Klöck, W., Arndt, P., et al. 1998, *M&PS*, **33**, 267
- Grima, C., Kofman, W., Mougnot, J., et al. 2009, *GeoRL*, **36**, L03203
- Hayatsu, R., Matsuoaka, S., Scott, R. G., Studier, M. H., & Anders, E. 1977, *GeCoA*, **41**, 1325
- Hayatsu, R., Winans, R. E., Scott, R. G., et al. 1980, *Sci*, **207**, 1202
- Hayes, J. M. 1967, *GeCoA*, **31**, 1395
- Hecht, M. H., Kounaves, S. P., Quinn, R. C., et al. 2009, *Sci*, **325**, 64
- Hoffman, J. H., Chaney, R. C., & Hammack, H. 2008, *JASMS*, **19**, 1377
- Hubbard, B., Milliken, R. E., Kargel, J. S., Limaye, A., & Souness, C. 2011, *Icar*, **211**, 330
- Isnard, R., Bardyn, A., Fray, N., et al. 2019, *A&A*, **630**, A27
- Janches, D., Bruzzone, J. S., Pokorný, P., Carrillo-Sanchez, J. D., & Sarantos, M. 2020, *PSJ*, **1**, 59
- Jenniskens, P. 2001, in *ESA SP-495, Proc. of Meteoroids Conf.*, ed. B. Warmbein (Noordwijk: ESA), 247
- Jessberger, E. K., Christoforidis, A., & Kissel, J. 1988, *Natur*, **332**, 691
- Keller, L. P., & Flynn, G. J. 2022, *NatAs*, **6**, 731
- Keppler, F., Vigano, I., McLeod, A., et al. 2012, *Natur*, **486**, 93
- Kerridge, J. F. 1983, *E&PSL*, **64**, 186
- Knutsen, E. W., Villanueva, G. L., Liuzzi, G., et al. 2021, *Icar*, **357**, 114266
- Kohout, T., Kallonen, A., Suuronen, J.-P., et al. 2014, *M&PS*, **49**, 1157
- Korablev, O., Vandaele, A. C., Montmessin, F., et al. 2019, *Natur*, **568**, 517
- Krasnopolsky, V. 2006, *Icar*, **185**, 153
- Krasnopolsky, V. A., Maillard, J. P., & Owen, T. C. 2004, *Icar*, **172**, 537
- Lefèvre, F., & Forget, F. 2009, *Natur*, **460**, 720
- Levin, G. V., & Straat, P. A. 1979a, *Natur*, **277**, 326
- Levin, G. V., & Straat, P. A. 1979b, *JMole*, **14**, 167
- Lewis, S. R., Collins, M., Read, P. L., et al. 1999, *JGR*, **104**, 24177
- Llamas, H. J., Aplin, K. L., & Berthoud, L. 2022, *P&SS*, **218**, 105517
- Lodders, K., & Fegley, B., Jr. 2011, *Chemistry of the Solar System* (Cambridge: RSC Publishing)
- Ming, D. W., Lauer, H. V., Archer, P. D., et al. 2009, *LPSC*, **40**, 2241
- Montmessin, F., Korablev, O. I., Trokhimovskiy, A., et al. 2021, *A&A*, **650**, A140
- Moore, J. E., Gough, R. V., Martinez, G. M., et al. 2019a, *NatGeo*, **12**, 321
- Moore, J. E., King, P. L., Smith, C. L., et al. 2019b, *GeoRL*, **46**, 9430
- Moore, J. E., Sapers, H. M., & Schuerger, A. C. 2024, *RNAAS*, **8**, 120
- Moore, J. E., & Schuerger, A. C. 2012, *JGRE*, **117**, E08008
- Moore, J. E., Smith, C. L., & Schuerger, A. C. 2017, *P&SS*, **147**, 48
- Moore, J. E., Smith, P. H., Tanner, R., Schuerger, A. C., & Venkateswaran, K. J. 2007, *Icar*, **192**, 417

- Navarro-González, R., Vargas, E., de la Rosa, J., Raga, A. C., & McKay, C. P. 2010, *JGRE*, **115**, E12010
- Nesvorný, D., Janches, D., Vokrouhlický, D., et al. 2011, *ApJ*, **743**, 129
- Nesvorný, D., Jenniskens, P., Levison, H. F., et al. 2010, *ApJ*, **713**, 816
- Nesvorný, D., Vokrouhlický, D., Bottke, W., & Sykes, M. 2006, *Icar*, **181**, 107
- Ojha, L., Nerozzi, S., & Lewis, K. 2019, *GeoRL*, **46**, 8671
- Patel, M. R., Berces, A., Keregyarto, T., et al. 2004, *AdSpR*, **33**, 1247
- Pokorný, P., Janches, D., Sarantos, M., et al. 2019, *JGRE*, **124**, 752
- Pokorný, P., Mazarico, E., & Schorghofer, N. 2021, *PSJ*, **2**, 85
- Pokorný, P., Sarantos, M., & Janches, D. 2017, *ApJL*, **842**, L17
- Pokorný, P., Sarantos, M., & Janches, D. 2018, *ApJ*, **863**, 31
- Poppe, A. R. 2016, *Icar*, **264**, 369
- Poppe, A. R., Lisse, C. M., Piquette, M., et al. 2019, *ApJL*, **881**, L12
- Potapov, A., Elisabetta Palumbo, M., Dionnet, Z., et al. 2022, *ApJ*, **935**, 158
- Rojas, J., Duprat, J., Engrand, C., et al. 2021, *E&PSL*, **560**, 116794
- Rowan-Robinson, M., & May, B. 2013, *MNRAS*, **429**, 2894
- Ruff, S. W., & Christensen, P. R. 2002, *JGRE*, **107**, 5127
- Saleh, R., Robinson, E. S., Ahem, A. T., & Donahue, N. M. 2017, *AerST*, **51**, 501
- Schuerger, A. C., Clausen, C., & Britt, D. 2011, *Icar*, **213**, 393
- Schuerger, A. C., Mancinelli, R. L., Kern, R. G., Rothschild, L. J., & McKay, C. P. 2003, *Icar*, **165**, 253
- Schuerger, A. C., Moores, J. E., Clausen, C. A., Barlow, N. G., & Britt, D. T. 2012, *JGRE*, **117**, E08007
- Sephton, M. A., & Botta, O. 2008, in *Strategies of Life Detection, Space Sciences Series of ISSI*, Vol. 25, ed. O. Botta et al. (Boston, MA: Springer), 25
- Sharma, S., Roppel, R. D., Murphy, A. E., et al. 2023, *Natur*, **619**, 724
- Steele, A., Benning, L. G., Wirth, R., et al. 2018, *SciA*, **4**, eaat5118
- Steininger, H., Goesmann, F., & Goetz, W. 2012, *P&SS*, **71**, 9
- Summers, M. E., Lieb, B. J., Chapman, E., & Yung, Y. L. 2002, *GeoRL*, **29**, 2171
- Tange, O. 2018, GNU Parallel, Zenodo, doi:10.5281/zenodo.1146014
- Taylor, S., Lever, J. H., & Harvey, R. P. 1998, *Natur*, **392**, 899
- Taylor, S., Matrajt, G., & Guan, Y. 2012, *M&PS*, **47**, 550
- ten Kate, I. L. 2018, *Sci*, **360**, 1068
- ten Kate, I. L., Garry, J. R. C., Peeters, Z., et al. 2005, *M&PS*, **40**, 1185
- Tomasko, M. G., Doose, L. R., Lemmon, M., Smith, P. H., & Wegryn, E. 1999, *JGR*, **104**, 8987
- Thomas, K. L., Keller, L. P., Blanford, G. E., & McKay, D. S. 1994, in *AIP Conf. Proc. 310, Analysis of Interplanetary Dust, Proceedings of the NASA / LPI Workshop*, ed. E. Zolensky et al. (Melville, NY: AIP), 165
- Vondrak, T., Plane, J. M. C., Broadley, S., & Janches, D. 2008, *ACP*, **8**, 7015
- Webster, C. R., Mahaffy, P. R., Atreya, S. K., et al. 2015, *Sci*, **347**, 415
- Webster, C. R., Mahaffy, P. R., Atreya, S. K., et al. 2018, *Sci*, **360**, 1093
- Witze, A. 2023, *Natur*, **622**, 439
- Wong, A., Atreya, S. K., & Encrenaz, T. 2003, *JGRE*, **108**, 5026
- Woodward, C. E., Wooden, D. H., Harker, D. E., et al. 2021, *PSJ*, **2**, 25
- Yang, H., & Ishiguro, M. 2015, *ApJ*, **813**, 87
- Zeng, X., Li, X., Wang, S., et al. 2015, *EP&S*, **67**, 72
- Zook, H. A. 2001, in *Accretion of Extraterrestrial Matter Throughout Earth's History*, ed. B. Peucker-Ehrenbrink & B. Schmitz (New York: Kluwer), 75